ISBN 978-82-471-3028-5 (printed ver.)
ISBN 978-82-471-3029-2 (electronic ver.)
ISSN 1503-8181




Doctoral theses at NTNU, 2011:234

Ruben Bjørge

# Scanning transmission electron microscopy studies of precipitation in Al-Mg-Ge alloys

**NTNU**
Norwegian University of
Science and Technology
Thesis for the degree of
philosophiae doctor
Faculty of Natural Sciences and Technology
Department of Physics

NTNU
Norwegian University of
Science and Technology

Doctoral theses at NTNU, 2011:234

NTNU

NTNU
Norwegian University of
Science and Technology

Ruben Bjørge

# Scanning transmission electron microscopy studies of precipitation in Al-Mg-Ge alloys

Thesis for the degree of Philosophiae Doctor

Trondheim, September 2011

Norwegian University of
Science and Technology
Faculty of Natural Sciences and Technology
Department of Physics

**NTNU – Trondheim**
Norwegian University of
Science and Technology

**NTNU**
Norwegian University of Science and Technology

Thesis for the degree of philosophiae doctor

Faculty of Natural Sciences and Technology
Department of Physics



ISBN 978-82-471-3028-5 (printed ver.)
ISBN 978-82-471-3029-2 (electronic ver.)
ISSN 1503-8181

Doctoral Theses at NTNU, 2011:234

Printed by Tapir Uttrykk

# Abstract

Precipitation in three Al-Mg-Ge(-Si-Cu) alloys has been investigated using transmission electron microscopy. The alloy compositions were chosen to be similar to previously studied Al-Mg-Si(-Cu) alloys to facilitate direct comparison. These alloys are strengthened by the precipitation of nanometre-sized, needle-shaped particles during heat treatment. A deeper understanding of precipitation at the atomic level is required in order to achieve greater control over alloy properties. The precipitation in the investigated Al-Mg-Ge(-Si-Cu) alloys was found to share similarities with that in Al-Mg-Si(-Cu) alloys, but there were also significant differences.

The high atomic number of Ge relative to Al, Mg, and Si made Al-Mg-Ge alloys highly suited for study by the atomic-number sensitive technique high-angle annular dark-field scanning transmission electron microscopy (HAADF STEM). This was the most important technique employed in this thesis. The use of a state-of-the-art aberration-corrected microscope also made it possible to resolve details previously inaccessible.

A near-hexagonal network of Ge columns when viewed along the needle direction was a unifying feature of all the precipitates in these alloys, as is the case in the metastable precipitates of the Al-Mg-Si(-Cu) alloy system. However, the $\beta''$ phase, the most important hardening phase in Al-Mg-Si alloys, was not observed. Instead, hardnesses similar to that of comparable Al-Mg-Si(-Cu) alloys were achieved through other precipitate phases.

Two Al-Mg-Ge alloys were the main objects of study in this thesis: one Mg-rich and one Ge-rich, with an addition of Mg and Ge in the relation $Mg_2Ge$ and $Mg_5Ge_6$, respectively. Precipitate phases that form in overaged Al-Mg-Si alloys were observed around peak hardness in these Al-Mg-Ge alloys, as well as disordered precipitates. The precipitate phases known from Al-Mg-Si, $U1$ and $\beta'$, were finer and more coherent with the Al matrix in the Al-Mg-Ge alloys than their counterparts in Al-Mg-Si. These precipitates also displayed highly interesting interface structures, consisting of Ge atoms in columns not part of the bulk precipitate structure.

The $\beta'$-like precipitate phase that was observed in the Mg-rich alloy was

investigated by quantitative HAADF STEM. This method makes it possible to obtain quantitative compositional information from the specimen. It was found that the Ge-rich columns contained significantly less Ge than the Si columns of $\beta'$ in Al-Mg-Si alloys. A partial replacement of Ge by Al or vacancies might explain the smaller lattice parameter of the $\beta'$-like phase in Al-Mg-Ge compared with $\beta'$ in Al-Mg-Si alloys.

Precipitation in an Al-Mg-Si-Ge-Cu alloy was also investigated with HAADF STEM. No repeating unit cell was observed in these precipitates near peak hardness. However, these precipitates contained a hexagonal network consisting of mixed Si and Ge columns with Mg, Al, and Cu columns occurring in between the network columns at specific sites. Structural units consisting of Al, Mg, Si, and Ge were often arranged in an ordered manner.

# Acknowledgements

First of all, I must thank my main adviser Professor Randi Holmestad. I am grateful for her support, for always having my best interests in mind, and for giving me the freedom to pursue what I found interesting in this work.

This work could truly not have been possible without the insight of Calin Mariora and Sigmund Andersen in SINTEF Materials and Chemistry. I thank them for sharing their enthusiasm for precipitation with me and for their great help in improving my manuscripts. I am in particular indebted to Calin for teaching me the intricacies of TEM of aluminium alloys, and to Sigmund for spending long hours poring over the images.

I thank the participants of the Nucleation control project for many memorable project meetings and for taking an interest in my work, and the members of the TEM group for making this journey an enjoyable one. It's been a great help to pursue this research in parallel with Malin Torsæter. Flemming Ehlers deserves special recognition for taking an interest in my results, even results that I did not fully appreciate the value of. I must also thank Associate Professor Anne Elster in the Department of Computer and Information Science, NTNU, for giving me access to the GPU resources of her lab.

I was fortunate to be able to spend seven months at Monash University in Melbourne, Victoria in the third year of my Ph.D. visiting the Monash Centre for Electron Microscopy and the Australian Research Council Centre of Excellence for Design in Light Metals. I am grateful for the hospitality extended to Amanda and me by the staff and students there. The results obtained there form the bulk of my thesis. I must thank Associate Professor Joanne Etheridge and Professor Barry Muddle for their interest in my work and all their input. I was impressed by the breadth and depth of the ongoing research at the two centres, and feel privileged to have been a part of it. I thank Philip Nakashima for being my main contact person, but most of all for sharing his enthusiasm for good science with me. I am grateful to Matthew Weyland and Christian Maunders for teaching me how to operate the Titan, and Christian Dwyer for sharing his knowledge of multislice

simulations.

I am grateful for the great friends I have been blessed with here in Trondheim and around the world, in particular our small group here in Trondheim. I also wish to thank my family and in-laws for their support over the years.

Finally, I must thank my wife Amanda for believing in me, and for her continual support and encouragement.

# Preface

This thesis is submitted in partial fulfilment of the requirements for the degree of philosophiae doctor at the Norwegian University of Science and Technology (NTNU). The doctoral work has been carried out at the Department of Physics, NTNU. The majority of the experimental results of this thesis were obtained during two visits to Monash University in Melbourne, Victoria, Australia.

The thesis is divided into two parts. The first part contains an introduction to the materials investigated in this work and the main experimental techniques used. The main conclusions and outlook are also given at the end of this part. Part II contains four scientific papers that constitute the most important portion of this thesis. Some of the experimental details of this work are omitted from Part I and instead described in the papers in Part II.

**Publications contained in this thesis**

- R. Bjørge, C. D. Marioara, S. J. Andersen and R. Holmestad
  *Precipitation in two Al-Mg-Ge alloys*
  Metallurgical and materials transactions A 41 (2010) 1907–1916.

- R. Bjørge, P. N. H. Nakashima, C. D. Marioara, S. J. Andersen, B. C. Muddle, J. Etheridge and R. Holmestad
  *Precipitates in an Al-Mg-Ge alloy studied by aberration-corrected scanning transmission electron microscopy*
  Acta Materialia 59 (2011) 6103–6109.

- R. Bjørge, S. J. Andersen, C. D. Marioara, J. Etheridge and R. Holmestad
  *Scanning transmission electron microscopy investigation of an Al-Mg-Si-Ge-Cu alloy*
  Submitted to Philosophical Magazine.

- R. Bjørge, C. Dwyer, M. Weyland, P. N. H. Nakashima, C. D. Marioara, S. J. Andersen, J. Etheridge and R. Holmestad
  *HAADF STEM study of $\beta'$-like preciptitates in an Al-Mg-Ge alloy*
  To be submitted.

Scientific research is a team effort, and the listed co-authors above have contributed either experimentally or through the interpretation of results. All the experimental and numerical work has been performed by myself, with the following exceptions: The high-resolution images in Paper I, except where noted, were acquired by C. D. Marioara. The STEM images in Paper II were acquired by P. N. H. Nakashima. The quantitative STEM images in Paper IV were obtained by M. Weyland.

**Other publications as first author**

- R. Bjørge, C. D. Marioara, S. J. Andersen and R. Holmestad. Journal of Electron Microscopy 59 (2010) S129–S133.

- R. Bjørge, P. N. H. Nakashima, C. D. Marioara, S. J. Andersen, B. C. Muddle, J. Etheridge and R. Holmestad. Aluminium alloys, Ed. by S. Kumai, O. Umezawa, Y. Takayama, T. Tsuchida and T. Sato, (Japan Institute of Light Metals 2010) 1391–1396.

- R. Bjørge, C. Dwyer, M. Weyland, P. N. H. Nakashima, J. Etheridge and R. Holmestad. Journal of Physics: Conference Series *submitted* (2011).

**Co-authored publications**

- S. J. Andersen, C. D. Marioara, R. Vissers, M. Torsæter, R. Bjørge, F. Ehlers and R. Holmestad. Materials Science Forum 638-642 (2010) 390–395.

- R. Holmestad, C. D. Marioara, F. J. H. Ehlers, M. Torsæter, R. Bjørge, J. Røyset and S. J. Andersen. Aluminium alloys, Ed. by S. Kumai, O. Umezawa, Y. Takayama, T. Tsuchida and T. Sato, (Japan Institute of Light Metals 2010) 30–39.

- S. J. Andersen, C. D. Marioara, M. Torsæter, R. Bjørge, F. J. H. Ehlers, R. Holmestad, O. Reiso and J. Røyset. Aluminium alloys, Ed. by S. Kumai, O. Umezawa, Y. Takayama, T. Tsuchida and T. Sato, (Japan Institute of Light Metals 2010) 413–419.

- H. Kauko, K. Muller, A. Rosenauer, R. Bjørge, R. Holmestad and A. T. J. van Helvoort. Journal of Physics: Conference Series *submitted* (2011).
- R. Holmestad, R. Bjørge, F. J. H. Ehlers, M. Torsæter, C. D. Marioara and S. J. Andersen. Journal of Physics: Conference Series *submitted* (2011).

In addition, I gave a talk at the European Microscopy Congress in Aachen, Germany in September, 2008 and presented a poster at the SuperSTEM Workshop in Daresbury, England in July, 2010. I also had the pleasure of attending the European workshop on advanced TEM measurement techniques for materials science (QEM 2009) in St. Aygulf, France in May, 2009.

Trondheim, September 2011

Ruben Bjørge

# Contents

# Part I

# Introduction

# Chapter 1

# Motivation

There is a desire in industry to extend the application of Al alloys to new areas. This typically requires alloys with improved properties. At the same time, there is a demand for greater control of Al alloy properties, in order to make it possible to tailor the material to its application, what is known as alloy design. Both necessitate a better understanding of Al alloys, in particular their strengthening mechanisms, but also corrosion-resistance, formability, and high-temperature stability. In Al-Mg-Si and related alloys, strength is acquired through the precipitation of nanometre-sized needle-shaped particles. Thus, these alloys need to be studied at the nanoscale. Determining the structure and composition of many of the precipitates that form has lead to important new insights into these alloys [1].

An interesting finding has been the similar arrangement of silicon atomic columns in all the metastable precipitates when viewed along the needle direction. These columns are arranged near-hexagonally with a projected unit cell with lattice parameters $a = b \approx 0.4\,\mathrm{nm}$ [2, 3]. With this apparent importance of Si in mind, this thesis investigates the precipitation of similar alloys, where the Si has been fully or partially replaced by germanium. Ge is situated directly below Si in the periodic table and the two elements are in many respects similar: both occur in the diamond structure and have strong directional bonds. Besides the aim of improving the properties of Al-Mg-Si alloys, Ge-replacement can lead to insight on precipitation in Al-Mg-Si alloys as well. For example, due to the significant difference in the atomic number of Ge on one hand, and Al and Mg on the other, the atomic-number sensitive imaging technique high-angle annular dark-field scanning transmission electron microscopy (HAADF STEM) allows these elements to be distinguished [4, 5].

Studying the precipitate/matrix interface is an active area of research

[6, 7, 8]. The interface is important because the coherency strain field surrounding a coherent interface increases the hardening effect of a precipitate, but also because the interface can play a role in determining the structure, growth, and composition of the precipitate [9]. HAADF STEM is ideally suited for studying interfaces because intensity maxima in the image correspond to atomic columns.

HAADF STEM has also recently been used to extract quantitative compositional information from the images [10, 11, 12]. A goal of this thesis was therefore to investigate the application of various aspects of STEM to precipitates. Precipitates are often small and embedded in the Al matrix, which make high-resolution imaging and structure determination difficult.

This Introduction consists of two main parts: one on aluminium alloys, in particular the materials and phenomena relevant to this thesis, and a second part on transmission electron microscopy, with an emphasis on the particular techniques used in this work. This chapter is followed by a summary of the conclusions that have been drawn in the papers in Part II, as well as possible topics to investigate moving forward.

# Chapter 2

# Aluminium alloys

Aluminium is the third most abundant element in the Earth's crust, after oxygen and silicon, and hence, the most abundant metal. Aluminium is too reactive to occur in its pure form in nature, and it therefore occurs naturally in different types of minerals. The most important aluminium ore is bauxite, named after the the French village Les Baux-de-Provence, where it was discovered in 1821. Bauxite is converted to alumina through the Bayer process. Aluminium can then be obtained from alumina through electrolysis in a process known as the Hall-Héroult process, invented independently in 1886 by Charles Hall and Paul Héroult. Before this, pure aluminium had been very difficult to extract. Aluminium was therefore more valuable than gold. It is told that Emperor Napoleon III once hosted a banquet where the most honoured guests were given aluminium utensils, while everyone else had to use gold or silver [13].

The electrolysis of alumina requires a large amount of electric current. Europe's first aluminium smelter was built in Switzerland near the Rhine waterfalls, which provided inexpensive hydroelectric power [13]. The access to hydroelectric power was also an important reason for starting aluminium production in Norway.

Aluminium has a face-centred cubic (fcc) unit cell, with lattice parameter $a = 4.05\,\text{Å}$. Pure aluminium is a weak material. The tensile strength of annealed pure aluminium is 47 MPa [14, p. 513]. However, if certain solute elements are added and suitable processing steps applied, medium to high-strength alloys with excellent properties can be made. The most important properties are: high strength, low weight, formability, corrosion resistance, weldability, recyclability, and high electrical and thermal conductivity. Aluminium alloys find numerous applications in buildings, packaging, aeroplanes, and automobiles. The alloy properties can to a certain degree be

Table 2.1: Overview of wrought aluminium alloy systems and common solute elements.

| Alloy system | Main solute elements | Other solute elements |
|---|---|---|
| 1xxx | $> 99\%$ pure Al | |
| 2xxx | Cu | Mg |
| 3xxx | Mn | |
| 4xxx | Si | |
| 5xxx | Mg | |
| 6xxx | Mg, Si | Cu |
| 7xxx | Zn | Mg, Cu |
| 8xxx | Special alloys | |

controlled through the alloy composition and thermo-mechanical treatment.

Aluminium alloys can be divided into two types: casting alloys and wrought alloys. Casting alloys are cast directly into their final form. Wrought alloys, on the other hand, are first cast and then worked into the desired form through extrusion, rolling, or other means. Wrought alloys are classified based on the solute atoms contained in the alloy. This is shown in Table 2.1. Wrought alloys can also be divided into two main groups: Heat treatable, or precipitation hardening, alloys (2xxx, 6xxx, and 7xxx), and non-heat treatable alloys (1xxx, 3xxx, 4xxx, and 5xxx).

The strength and hardness of an aluminium alloy are measures of its resistance to plastic deformation. Plastic deformation, in which atomic bonds are broken and reformed, is caused by the movement of one-dimensional lattice defects known as dislocations. There are, in general, four strengthening mechanisms in aluminium alloys [14]. These are: strain hardening, solute hardening, grain size hardening, and precipitation hardening. Strain hardening, also known as work hardening, works by straining the material which increases the dislocation density. The movement of a dislocation is hindered by the presence of other dislocations. In solute hardening, a solute element with a size different from Al deforms the matrix. This deformation hinders dislocation motion leading to hardening. This is an important mechanism in 5xxxx alloys. Grain size, or microstructure, hardening depends on the fact that the strength of an aluminium alloy is inversely proportional to the grain size [15, 16]. Since neighbouring grains typically have different orientations, the movement of dislocations is hindered by the grain boundaries. This is known as Hall-Petch hardening, after its discoverers. Precipitation,

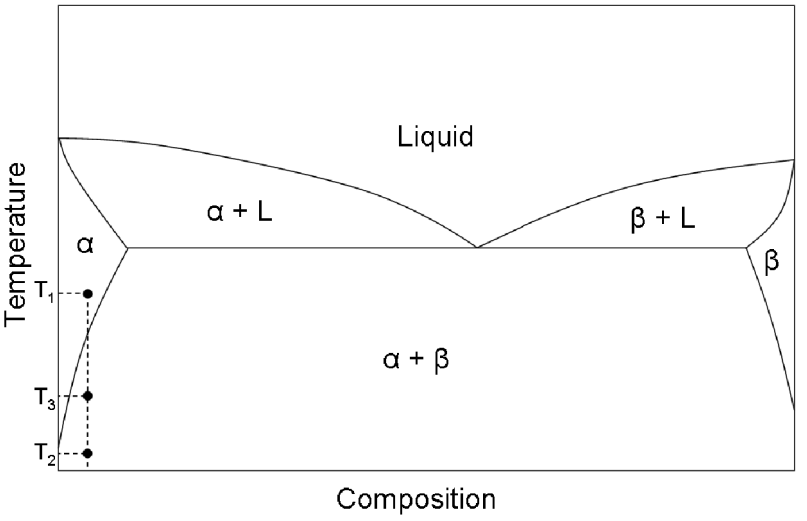


Figure 2.1: A schematic binary eutectic phase diagram.

or age hardening gives the strongest aluminium alloys, and is the main strengthening mechanism in 6xxx series alloys, the topic of this thesis.

Age hardening was discovered by accident in 1906 by Alfred Wilm, in an Al-Cu-Mg-Mn alloy [17, 1], when he left it over the weekend and did the hardness testing on the following Monday. That the increase in hardness was the result of precipitation, was first proposed in 1919 by Merica et al. [18]. This was controversial, however, since no precipitates could be observed until long after the onset of hardening, with the microscopes available at the time [19]. The presence of precipitates was first proven by Guinier and Preston in 1938 by x-ray scattering [20, 21].

In precipitation hardening, small particles that have precipitated from solid solution hinder the movement of dislocations. A prerequisite for precipitation hardening is that the solid solubility of the solute elements must vary with temperature: it must be relatively large at a temperature that is high but below the melting temperature of Al, and low at room temperature. This can be seen in the schematic binary phase diagram shown in Figure 2.1. During solution heat treatment, the alloy is heated to a temperature, $T_1$, above the solvus line in the phase diagram. Here the aluminium and solute elements coexist in a solid solution, meaning the solute elements are distributed uniformly in the aluminium matrix (the phase $\alpha$). Heating the alloy also increases the vacancy concentration since this has an exponential dependence on temperature [22].

The alloy is then rapidly quenched to a temperature, $T_2$, well below the solvus line, typically room temperature. Quenching creates what is known as a supersaturated solid solution (SSSS), since the solute concentration in the matrix is much higher than the equilibrium concentration at room temperature. At room temperature, the other equilibrium phase $\beta$, is not able to form due to low diffusion rates. Quenching also creates a large number of vacancies that are trapped inside the matrix.

The alloy is then typically heated to an intermediate temperature, $T_3$, for ageing. Instead of forming the equilibrium phase $\beta$, other phases that are not part of the equilibrium phase diagram precipitate in the Al matrix. These are known as metastable phases since they cannot form outside the Al matrix. The bulk energy of these phases is higher than for the equilibrium phase. However, this is compensated for by a lower interfacial energy between the metastable phase and matrix, due to a greater degree of coherency.

During ageing, solute atoms move toward each other, aided by the quenched-in vacancies. The types of precipitates that form depend on the ageing temperature and the duration of the ageing. At the early stages of ageing, atomic clusters form on the aluminium matrix. At elevated temperatures, Guinier-Preston (GP) zones form. These are fully coherent with the Al matrix. The hardness of the alloy increases because more stress is needed for dislocations to move through the GP zones [22]. Upon further ageing, peak hardness is reached. Peak hardness is typically characterized by phases that are coherent with the matrix, but that have some degree of misfit. The lattice mismatch increases the hardness because dislocation movement is now also hindered by the strain field surrounding the precipitate. With further ageing the number density of precipitates decreases as well as the degree of coherence. This leads to a decrease in hardness since it becomes easier for the dislocations to bow around the precipitates [22]. At a high enough ageing temperature the equilibrium precipitate phase eventually forms.

## 2.1 Precipitation in 6xxx alloys

Because of their high strength, good formability, and corrosion resistance, 6xxx alloys constitute an industrially important group of materials with the main applications in transportation and construction. Recently, this alloy system has found increased use in automotive applications. The alloy must first be ductile when stamped into the desired shape, and then after a final heat treatment at approximately 180 °C, it must be much stronger [23].

The main alloying elements of 6xxx alloys are silicon and magnesium. This alloy system therefore conforms to the (±)-rule, since it has one atomic

species larger than Al (Mg), and one smaller (Si), as do other important ternary alloys such as Al-Cu-Mg and Al-Zn-Mg [24]. Copper can be added, resulting in higher strength, but less corrosion resistance [25]. The first Al-Mg-Si alloy introduced was 6051 in 1921 [1]. The equilibrium phase in the Al-Mg-Si alloy system is known as $\beta$ [26]. This phase has an anti-fluorite structure with composition $Mg_2Si$. It precipitates as plates parallel to $\{100\}_{Al}$. Precipitation in Al-Mg-Si alloys has been called the most perplexing of all the aluminium alloys [1]. The precipitation sequence in Al-Mg-Si alloys can be given as [27, 28]:

$$\begin{aligned}\text{SSSS} \rightarrow \begin{matrix}\text{Clusters of Si atoms}\\ \text{Clusters of Mg atoms}\end{matrix} &\rightarrow \text{Mg/Si co-clusters}\\ &\rightarrow \text{GP-zones} \rightarrow \beta'' \rightarrow \beta', U1, U2, B' \rightarrow \beta, \text{Si}.\end{aligned}$$

The clusters that first form out of solid solution are monatomic, consisting either of Mg or Si. This is followed by co-clusters consisting of both Mg and Si. GP-zones are the first precipitates that form. These are coherent with the Al matrix, and the atoms are close to the fcc positions of the matrix. GP-zones have been reported to be spherical in shape [29], but Marioara et al. have reported a needle-shaped $\beta''$ pre-cursor with a monoclinic unit cell [30]. GP-zones in the form of plates one atomic layer thick have been observed in a Al-1.6 weight percent $Mg_2Si$ alloy [31]. There is therefore some ambiguity in the term GP-zones as it relates to Al-Mg-Si alloys [28].

The $\beta''$ phase and the proceeding metastable phases (i.e., the phases preceding $\beta$) all precipitate as needles or rods growing along $\langle 001\rangle_{Al}$. These phases were originally assumed to have the same composition as $\beta$ [1]. This idea has, with the advent of advanced electron microscopy techniques and atom probe tomography, had to be thoroughly revised.

The $\beta''$ phase is found at peak hardness, and is considered the most important hardening phase in 6xxx alloys. It is needle-shaped with a typical size of $4\times4\times50\,\text{nm}^3$ [32]. Quantitative electron diffraction results suggested that this phase has the composition $Mg_5Si_6$ [32], but later studies combining atom probe tomography and density functional theory show that a composition of $Mg_5Al_2Si_4$ is more likely [33]. Formation of $\beta''$ requires an ageing temperature above at least 100 °C [34].

In overaged conditions, the $\beta'$, $U1$, $U2$, and $B'$ phases may precipitate. $U1$, $U2$, and $B'$ are also known as type-A, type-B, and type-C precipitates, respectively [35]. These are much coarser than $\beta''$, and are incoherent in the plane perpendicular to the needle direction. The relative abundance of these phases depends on the alloy composition and the heat treatment [36].

Table 2.2: Overview of precipitate phases in the Al-Mg-Si alloy system.

| Name | Space group | Lattice parameters | Composition | References |
|---|---|---|---|---|
| $\beta''$ | $C2/m$ | $a = 15.16\,\text{Å}$, $b = 4.05\,\text{Å}$, $c = 6.74\,\text{Å}$, $\beta = 105.3°$ | $Mg_5Al_2Si_4$ | [32, 33] |
| $\beta'$ | $P6_3/m$ | $a = 7.15\,\text{Å}$, $c = 12.15\,\text{Å}$, $\gamma = 120°$ | $Mg_9Si_5$ | [28] |
| $U1$ | $P\bar{3}m1$ | $a = 4.05\,\text{Å}$, $c = 6.74\,\text{Å}$, $\gamma = 120°$ | $MgAl_2Si_2$ | [2] |
| $U2$ | $Pnma$ | $a = 6.75\,\text{Å}$, $b = 4.05\,\text{Å}$, $c = 7.94\,\text{Å}$ | MgAlSi | [37] |
| $B'$ | $P\bar{6}$ | $a = 10.4\,\text{Å}$, $c = 4.05\,\text{Å}$, $\gamma = 120°$ | $Mg_9Al_3Si_7$ | [36] |
| $\beta$ | $Fm\bar{3}m$ | $a = 6.39\,\text{Å}$ | $Mg_2Si$ | [26, 38] |
| Si | $Fd\bar{3}m$ | $a = 5.43\,\text{Å}$ | Si | [38] |

An overview of the precipitate phases in the Al-Mg-Si system is given in Table 2.2.

$\beta'$ is a hexagonal phase that precipitates as needles with dimensions $\approx 10 \times 10 \times 500\,\text{nm}^3$ [28]. Its hexagonal crystal system was first deduced by Jacobs [26]. Later studies confirmed this [39], and a crystal structure was proposed [40]. A more detailed study combining quantitative electron diffraction and *ab initio* atomistic calculations determined the composition to be $Mg_9Si_5$ [28].

The hexagonal axis of $\beta'$ is parallel to the needle direction. For relatively small $\beta'$ precipitates, the orientation relationship between precipitate and matrix can be described as [28]:

$$\langle 001 \rangle_{\text{Al}} \parallel [001]_{\beta'} \text{ and } \langle 310 \rangle \parallel [100]_{\beta'}\,. \tag{2.1}$$

Other orientation relationships have also been reported in the cross-section plane of the precipitate needles [41]. Interestingly, the periodicity along the rod direction is not equal to the Al lattice parameter, but the triple of this (12.15 Å). This is due to the fact that the Si columns in the corner of the unit cell, shown in Figure 2.2, are not fully coherent with the matrix along the $c$-direction.

The phase that in this thesis is labeled $U1$ was first reported by Matsuda et al. in an excess-Si alloy [42]. It was reported to be hexagonal with lattice

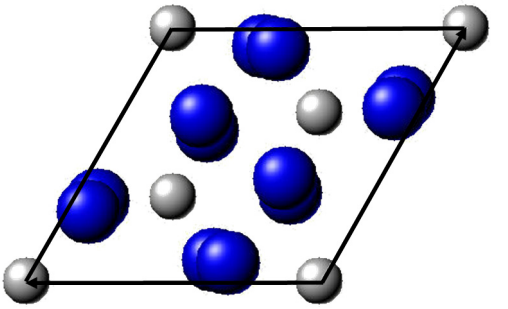

(a) Down hexagonal axis

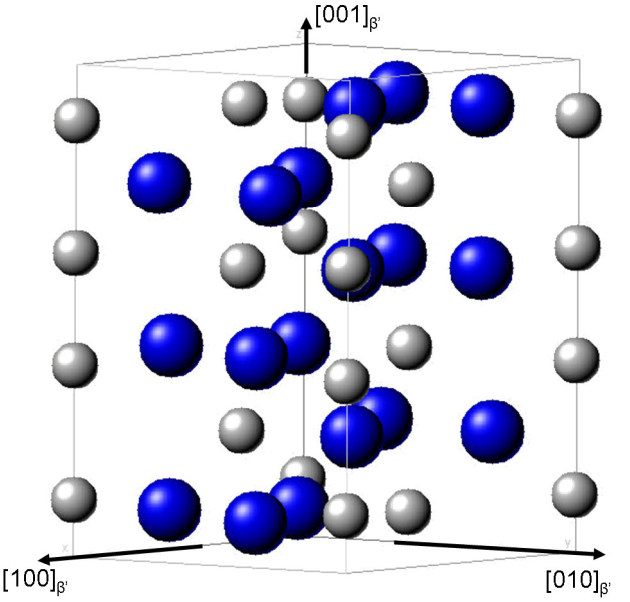


(b) Side view

Figure 2.2: Model of the hexagonal $\beta'$ phase seen down the hexagonal axis and from the side. The Mg atoms are blue and the Si atoms grey.

parameters $a = 4.05\,\text{Å}, c = 6.7\,\text{Å}$. This phase was later given the name 'type-A' and a composition of $MgAl_4Si_5$ was proposed [35]. The structure was later solved using a combination of *ab initio* atomistic calculations and quantitative electron diffraction [43, 2]. It was determined to be trigonal with a composition of $MgAl_2Si_2$. The precipitates are rod-like with widths of 50 nm and lengths 50–500 nm [43].

$U1$ differs from the other metastable phases in having the main axis of symmetry, $c$, perpendicular to the needle direction. $U1$ is found in two common orientations: $c \parallel \langle 310 \rangle_{\text{Al}}$ and $c \parallel \langle 110 \rangle_{\text{Al}}$ [2]. A $\langle 110 \rangle_{U1}$ direction is parallel with the needle direction and $\langle 001 \rangle_{\text{Al}}$ in both cases. $U1$ occurs in higher numbers in alloys that are Si-rich, which is reasonable since the phase itself contains more Si than Mg. A model of the $U1$ unit cell is shown in Figure 2.3. When viewed along the needle direction, the projection of the unit cell will be rectangular with dimensions 6.74 Å and 3.51 Å.

$U2$ phase has an orthorhombic structure [37, 35]. Its unit cell has the composition $Mg_4Al_4Si_4$. It occurs in overaged conditions, typically before $U1$ and $B'$ are formed [44].

The structure of the $B'$ phase [45], also known as type-C [35] or M [46], has not been published. However, a likely composition of $Mg_9Al_3Si_7$ has been determined using density functional theory [47]. The structure is suspected to be isostructural with the $Q$ phase in Al-Mg-Si-Cu alloys [36]. The $B'$ phase often precipitates heterogeneously in the Al matrix [35].

Adding copper to Al-Mg-Si alloys will typically increase their strength. In this case, the precipitation sequence is modified. The equilibrium phase is now the hexagonal $Q$ phase [48]. The $\beta''$ phase still appears, but other precipitate phases are also present at peak hardness. The precipitation sequence can be given as [3]:

$$\text{SSSS} \rightarrow \text{Atomic clusters} \rightarrow \text{GP-zones} \rightarrow \beta'', L, S, C, QC, QP \rightarrow \beta', Q' \rightarrow Q.$$

An overview of the precipitate phases unique to the Al-Mg-Si-Cu system is given in Table 2.3.

Marioara et al. found that the $\beta''$ and pre-$\beta''$ phases only made up 20-30% of the precipitates at peak hardness [3]. They found three so-called $Q'$ precursors present at peak hardness: L, S, and C. These phases typically precipitate in the shape of laths, i.e., needles with elongated cross sections. The L phase was first reported by Sagalowicz et al. [49]. Its cross section is elongated along $\langle 100 \rangle_{\text{Al}}$. Chakrabarti and Laughlin suggested that this phase is responsible for the increased strength of Al-Mg-Si-Cu alloys, relative to the Cu-free alloys [44]. The $S$ phase has its cross-section elongation parallel to $\langle 510 \rangle_{\text{Al}}$. This phase should not be confused with the $S$ phase

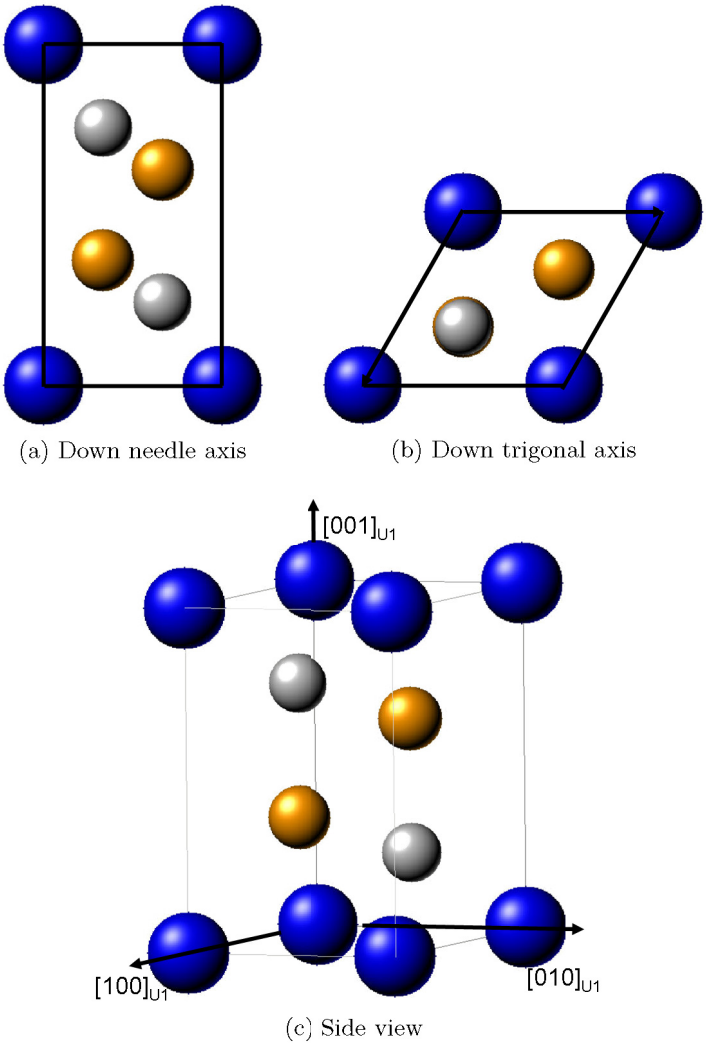


(a) Down needle axis (b) Down trigonal axis

(c) Side view

Figure 2.3: Model of the trigonal $U1$ phase seen down the needle axis, $[100]_{U1}$, down the trigonal axis, $[001]_{U1}$, and from the side. The Mg atoms are blue, Al atoms are orange, and the Si atoms grey.

Table 2.3: Overview of precipitate phases unique to the Al-Mg-Si-Cu alloy system.

| Name | Space group | Lattice parameters | Composition | References |
|---|---|---|---|---|
| $L$ | Unknown | Unknown | Unknown | [49, 44] |
| $S$ | Unknown | Unknown | Unknown | [3] |
| $C$ | Monoclinic | $a = 10.32\,\text{Å}$, $b = 8.1\,\text{Å}$, $c = 4.05\,\text{Å}$, $\gamma = 101°$ | Unknown | [3] |
| $QP$ | Hexagonal | $a = 3.93\,\text{Å}$, $c = 4.05\,\text{Å}$, $\gamma = 120°$ | Unknown | [50] |
| $QC$ | Hexagonal | $a = 6.70\,\text{Å}$, $c = 4.05\,\text{Å}$, $\gamma = 120°$ | Unknown | [50] |
| $Q'$ | Probably $P\bar{6}$ | $a = 10.4\,\text{Å}$, $c = 4.05\,\text{Å}$, $\gamma = 120°$ | Probably $Al_3Cu_2Mg_9Si_7$ | [51, 52, 44] |
| $Q$ | $P\bar{6}$ | $a = 10.39\,\text{Å}$, $c = 4.02\,\text{Å}$, $\gamma = 120°$ | Probably $Al_3Cu_2Mg_9Si_7$ | [48, 52] |

($CuMgAl_2$) occurring in Al-Cu-Mg alloys [53]. The $L$ and $S$ phases were both observed to be disordered. The $C$ phase had a cross section with a much higher aspect ratio and was therefore labeled as a 'plate-type' precipitate. This phase was found to be ordered with a monoclinic unit cell with lattice parameters $a = 10.32\,\text{Å}, b = 8.1\,\text{Å}, c = 4.05\,\text{Å}, \gamma = 101°$.

The $QC$ and $QP$ phases were reported by Cayron and coworkers [50, 40, 54] in composites based on a 2xxx alloy reinforced with $Al_2O_3$-$SiO_2$ fibres or SiC particles. The phases were both found to be hexagonal, with $a = 6.70\,\text{Å}$ for $QC$, and $a = 3.93\,\text{Å}$ for $QP$. The alloy investigated had the composition Al–4% Cu–0.7% Si–1% Mg–0.5% Ag (weight %), which is much more Cu-rich than typical Al-Mg-Si-Cu alloys.

$Q'$, the precursor of the equilibrium phase $Q$, is found mainly in the overaged stage [44, 3]. Its exact structure is not known, but its crystal system is hexagonal and its lattice parameters have been measured to be $a = 10.32\,\text{Å}, c = 4.05\,\text{Å}, \gamma = 120°$ It is thought to be similar in composition to the $Q$ phase. The two phases are isostructural, except that $Q'$ is coherent with the Al matrix along the needle direction.

Structural similarities between the different phases in Al-Mg-Si(-Cu) alloys were first described in detail by Cayron et al. [50]. They found that

many of the precipitates shared a common sublattice, with dimensions equal to the $QP$ phase. This included the Cu-containing precipitates $Q$, $Q'$, and $QC$, but also the Al-Mg-Si precipitates $U2$, and $B'$, through its connection with $Q'$. They also speculated that a sublattice model applicable to $\beta'$ and $\beta''$ could exist as well. These results were, however, mainly geometrical since the lattice parameters were considered, and not the atomic arrangement within the unit cell.

Through determining the atomic structure for all of the precipitates in the Al-Mg-Si alloy system, a link between the phases was found in the arrangement of Si. All the metastable precipitates were found to share a similar arrangement of Si columns, named the 'Si network,' when viewed along the needle direction [2]. This Si network is hexagonal or near-hexagonal, depending on the precipitate phase, with lattice parameter $a \approx b \approx 4\,\text{Å}$, which is close to the lattice parameter of $QP$ reported by Cayron et al. [50]. The same network was found to apply to the phases found in Al-Mg-Si-Cu alloys as well [3].

The precipitates can be seen as different arrangements of Al, Mg, and Cu on this network. The $U1$ phase is unique in having both a near-hexagonal arrangement of Si columns when viewed along the needle direction, but also a hexagonal arrangement of Si when viewed along the $c$-direction, which is parallel to a $\langle 310 \rangle_{\text{Al}}$ direction. In Figure 2.4, models of the metastable precipitate phases in Al-Mg-Si alloys are shown. The Si network is connected with dotted lines.

In this thesis, alloys where Si has been fully or partially replaced by Ge are studied. Pure germanium forms, just like Si, in a diamond structure. Germanium also forms as $Mg_2Ge$ with the same anti-fluorite structure as $\beta$. Ge and Si might therefore be expected to behave similarly as a solute element in Al. This is supported by the presence of GeSi precipitates in Al-Si-Ge alloys [55, 56]. Ge has a larger atomic radius than Si and Al. Al-Mg-Ge alloys do therefore not comply with the (±)-rule. Also, the diffusion rates are different for the two elements. At room temperature, Si diffuses more quickly than Ge, but at elevated temperatures, Ge is the quickest diffuser [57].

The earliest published investigations of Al-Mg-Ge alloys are from the 1960's [58, 59]. These were both studies of pre-precipitation clustering studied by x-ray diffraction and conductivity measurements. Suzuki et al. investigated the ageing behaviour of Al-Mg-Ge alloys using TEM [60]. They found the precipitation sequence to be similar to that of Al-Mg-Si alloys. Matsuda et al. have recently investigated precipitation in Al-Mg-Ge alloys [61, 62]. They found precipitates with the same structure as $\beta'$ and $U1$ in

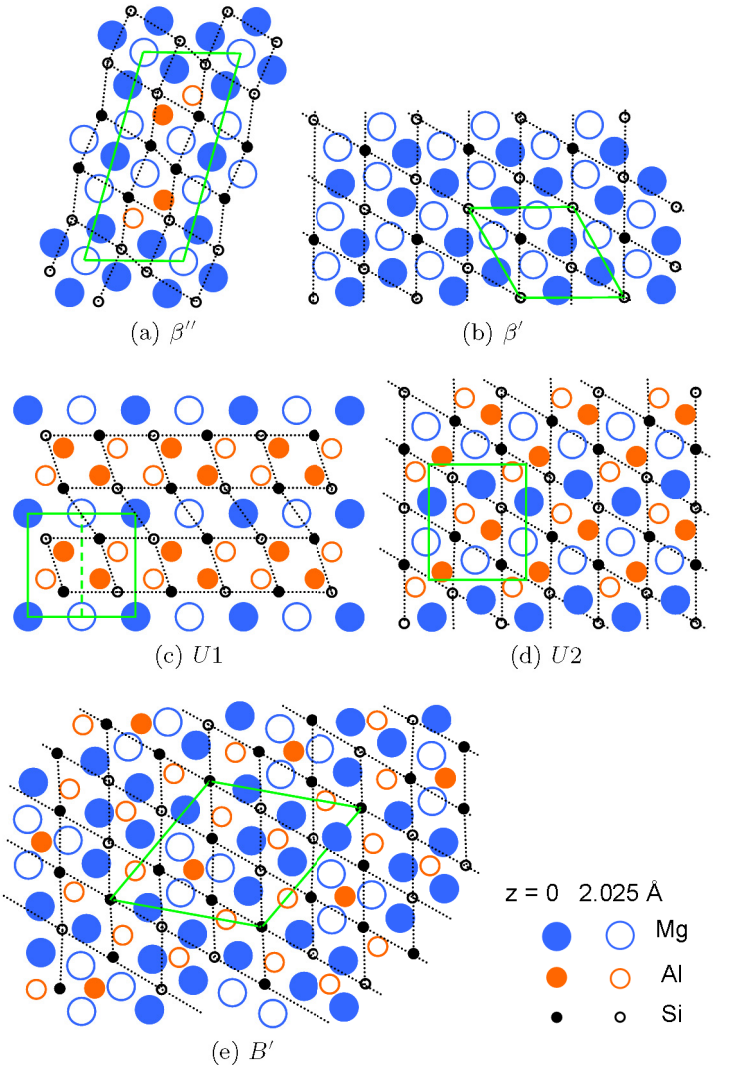


Figure 2.4: Model of precipitates in Al-Mg-Si alloys. The Si network is shown with dotted lines and unit cells with green lines.

these alloys.

Ringer et al. have recently investigated an Al-Cu-Mg alloy with a small addition of Ge [63]. They found that the addition of Ge lead to a refinement of the distribution of $\theta'$ precipitates, and observed lath-shaped precipitates composed of Mg and Ge. The addition of Ge also produced an internal structure within the $\theta'$ precipitates that was very similar to the $U1$ structure described above.

# Chapter 3

# Transmission electron microscopy

The electron was identified as a particle in 1897 by J. J. Thomson [64]. The electron's wave-like properties were discovered through electron diffraction experiments conducted independently by his son, G. P. Thomson, and C. J. Davisson in 1927. This was three years after de Broglie formulated his equation for the wavelength of matter waves. Busch showed in 1926 that electrons can be focused by electromagnetic fields, much like a glass lens can focus light [65]. The first electron microscope was built by Max Knoll and Ernst Ruska in 1932. A year later, the resolution had improved to 50 nm, with a magnification of 12000 [66]. Ruska was awarded half of the Nobel Prize in Physics for these achievements in 1986.

Today, transmission electron microscopy (TEM) is a powerful technique for studying materials on a length scale from ångströms to micrometers ($10^{-10}$–$10^{-6}$ m). It can be used for imaging and diffraction, as well as obtaining analytical (i.e., chemical) information. The great resolving power of TEM comes from the short wavelength of the high-energy electrons used. The wavelength of an electron accelerated through a potential of 200 kV is 0.02705 Å and at 300 kV, 0.01969 Å, compared with a typical atom radius of 1 Å. The resolution of a standard microscope though is about 2 Å, due to the imperfections of the electromagnetic lenses used. The advent of aberration-corrected TEMs has improved the resolution to below 1 Å. This might seem like a small improvement, but the increase in the amount of information accessible is enormous.

A schematic layout of a TEM is shown in Figure 3.1. The electrons are emitted at the top from an electron gun and accelerated through a potential (not shown). Two or more lenses known as condenser lenses placed above

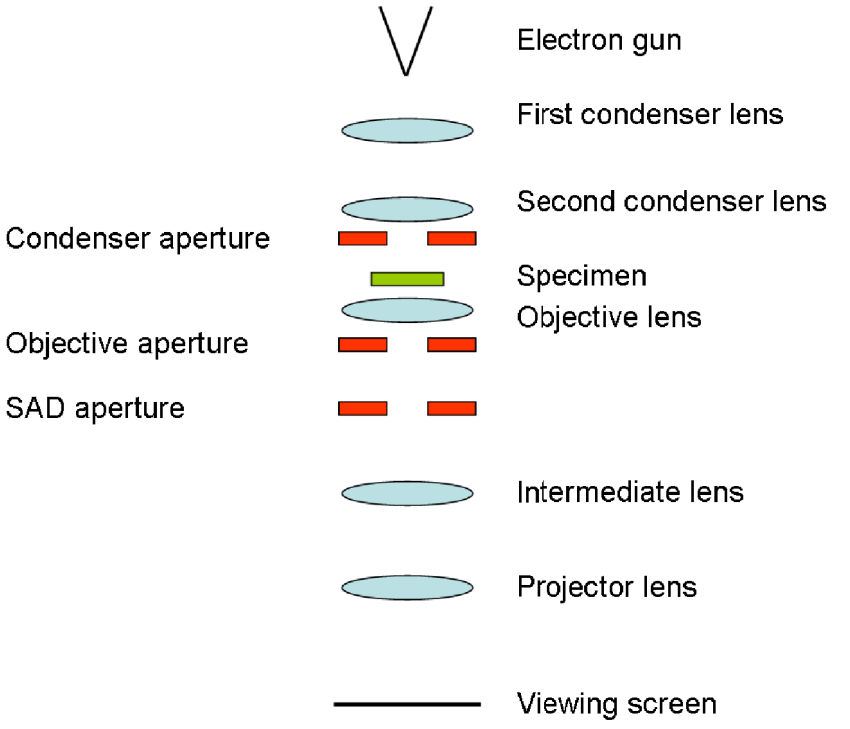


Figure 3.1: Schematic drawing of a TEM.

the specimen are responsible for forming the beam that illuminates the specimen. The objective lens forms the first image of the specimen, which is then magnified further by the intermediate and projector lenses onto a viewing screen or camera.

A TEM can be operated in two basic modes: imaging and diffraction. In each case the specimen is illuminated by an approximately parallel beam of electrons. As can be seen in Figure 3.2, rays that originate from the same part of the specimen are brought together in the image plane below the objective lens, essentially magnifying the specimen. Rays that have the same *direction* leaving the specimen are focused to a point in the back-focal plane of the objective lens. In imaging mode, the intermediate lenses of the microscope transfer the image in the image plane to the viewing screen, while in diffraction mode, the diffraction pattern in the back-focal plane appears on the screen.

Various imaging modes are possible by inserting an aperture in the back-focal plane, known as an objective aperture. One method is to only let the

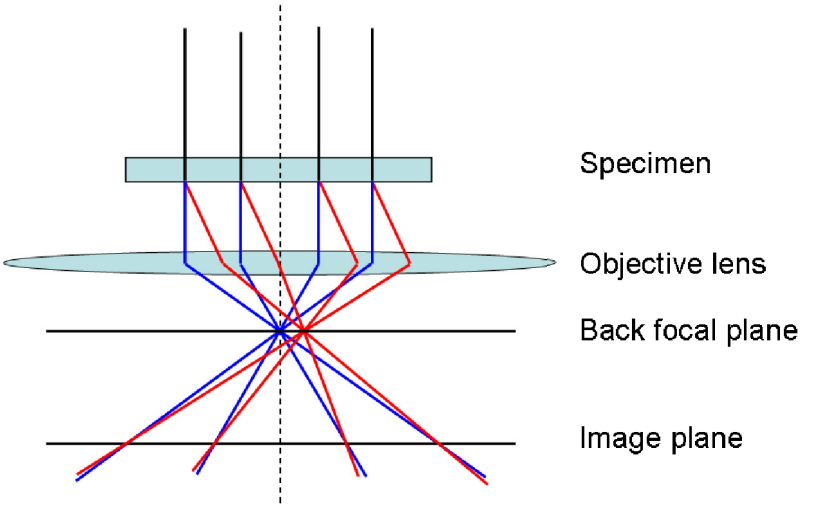


Figure 3.2: Schematic drawing illustrating the image and diffraction modes in a TEM. The blue beams are unscattered, while the red beams have been scattered by the same set of parallel planes. The optical axis is shown with a dashed vertical line.

central, undiffracted, beam contribute to the image. This is known as bright-field TEM. An image formed by using the objective aperture to select a diffracted beam is called a dark-field image. An aperture can also be inserted in the image plane to select the area that contributes to the diffraction pattern. This is known as a selected-area diffraction pattern (SADP).

Two important methods used in this thesis are high-resolution TEM (HRTEM) and scanning transmission electron microscopy (STEM). The STEM mode is shown in Figure 3.3. In HRTEM, many beams in the back-focal plane are allowed to interfere in the imaging plane. This image plane is then further magnified before it reaches the viewing screen or camera. The inclusion of the diffracted beams increases the resolution of the image since these contain high spatial frequency information. The focusing action of the objective lens happens *after* the specimen. In STEM, a converged beam is scanned across the specimen. Detectors, that can have different geometries, are placed far away from the specimen. In principle, no lenses are required after the specimen; the focusing happens *before* the specimen.

In a typical modern TEM the specimen sits inside the objective lens. The lens that focuses the unscattered electrons (the direct beam) into the same point in the back focal plane in TEM and HRTEM, is therefore the

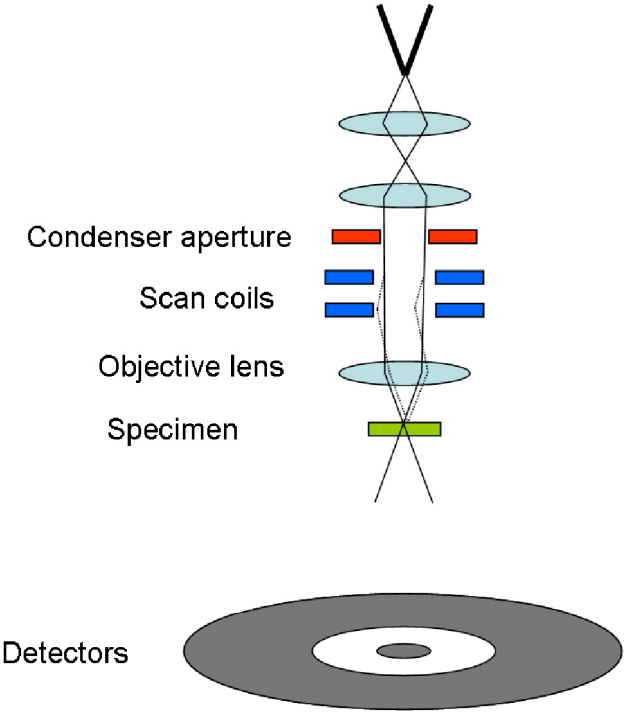


Figure 3.3: Schematic drawing of a STEM.

same lens that forms a focused probe on the entry surface of the specimen in STEM. Hence, the task of the objective lens, to focus the electron beams to form an image, is the same in each mode, but it happens after and before the specimen in TEM and STEM, respectively. Similarly, the objective aperture in HRTEM plays a role similar to the condenser aperture in STEM. Because of this similarity, many phenomena applicable to HRTEM and STEM can be explained without referring to a specific mode. This reciprocity will be discussed further in the section on STEM.

## 3.1 Limits to the resolution

The point resolution of a TEM can be described as the minimum separation at which two points can be resolved, i.e., distinguished. Although the wavelength of the electrons used in TEM is of the order of picometres, the achievable resolution is considerably poorer than this. The factors limiting the resolution can be divided into three: the aperture, lens aberrations, and incoherence [67].

An aperture placed in the focal plane of an objective lens will limit the angular range, or equivalently, the spatial frequency, of the rays that contribute to an image. This means that a point object will be imaged as an Airy pattern consisting of an intense central disc surrounded by concentric lobes. Taking the first zero of the pattern as the size of the disc, the point object is smeared out to a size, $\delta_D$, given by [67]:

$$\delta_D = 0.61\frac{\lambda}{\alpha}, \tag{3.1}$$

where $\lambda$ is the electron wavelength and $\alpha$ is the aperture semi-angle. This shows that the resolution increases with a larger aperture and a shorter wavelength. The limit of the resolution due to the aperture is known as the diffraction limit. An aperture in the focal plane of the objective lens is typically used to limit the effect of (other) aberrations. These aberrations are not inversely proportional to the aperture semi-angle.

The most limiting aberrations, or non-ideal imaging characteristics, are those of the objective lens. The effect of the lens aberrations can be expressed as a transfer function given by $\exp[\mathrm{i}\chi(\vec{k})]$. $\chi$ is known as the aberration function. The lens aberrations therefore give a phase shift to the different spatial frequencies, $\vec{k}$, that constitute the electron wave. In a non-aberration-corrected TEM, the most important lens aberrations are the spherical aberration, $C_s$, and the defocus, $\Delta f$. $\chi$ can then be expressed as:

$$\chi = \pi\lambda\Delta f k^2 + \frac{1}{2}\pi C_s\lambda^3 k^4. \tag{3.2}$$

Here, underfocus corresponds to a negative $\Delta f$. There is also another aberration, two-fold astigmatism, which causes a circle to be drawn out into an ellipse. This aberration is, however, easily corrected.

For an aberration-, or $C_s$-, corrected microscope, the spherical aberration coefficient is much smaller and higher-order terms must be included in this expression. The greatest advancement in the increase of resolution in TEM and STEM over the last decade is due to the use of aberration correctors that correct for this spherical aberration. Scherzer was the first to note that the rotationally symmetric electromagnetic lenses used in TEMs will always have a positive spherical aberration [68]. This means, in the geometrical optics view, that rays travelling farther from the optical axis are focused too strongly relative to rays closer to the optical axis.

A viable solution to the problem was proposed by Rose [69] and implemented by Haider et al. [70]. The spherical aberration corrector consists of two electromagnetic hexapoles. The first hexapoles introduces three-fold astigmatism, which is corrected by the second hexapoles, but a negative spherical aberration is also introduced [71]. This negative spherical aberration is used to compensate for the positive spherical aberration of the rest of the imaging system. Other methods for correcting the spherical aberration using different magnetic multipoles exist, but this is the method used in the FEI Titan$^3$ microscope used in this thesis.

The lens aberrations considered so far are known as geometrical aberrations. They are *coherent*, meaning that there remains a constant phase relation between different parts of the wave. Coherence implies no loss of information. There are also *incoherent* effects that must be considered. These can be divided into two: temporal incoherence and spatial incoherence [67]. The first is due to the spread in energy of the electrons. Due to the chromatic aberrations of the lens, electrons with different energies that enter the lens at the same point will be focused differently. Spatial incoherence is a term used for other incoherent aberrations that are not related to the energy of the incident electrons. Mechanical vibrations reduce the spatial coherence and are applicable to both HRTEM and STEM, while some aberrations are specific to either HRTEM or STEM. For example, the convergence angle of the nearly-parallel incident beam and the point-spread function of the camera is important to HRTEM, while the finite size of the electron source is important to STEM.

## 3.2 High-resolution transmission electron microscopy

In HRTEM, an approximately parallel beam of electrons illuminates the entrance surface of the specimen. At the exit surface of a crystalline specimen we find that the electrons have been scattered into many beams. What happens inside the specimen is clearly highly complicated and should be treated using the theory of dynamical diffraction in which the electron wave inside the specimen is described as the superposition of many Bloch states [72, 73]. Determining the crystal structure from the exit wave is not necessarily simple. In HRTEM however, the specimen area imaged is often so thin that dynamical effects can be ignored. At any rate, the main features of HRTEM are most easily explained for thin specimens.

For a thin specimen, the effect of the specimen on the incident electron wave, $\psi_{\text{inc}}(\vec{x})$, can be described as multiplication with a transmission function, $t(\vec{x})$ [74]:

$$\psi_{\text{ex}} = t(\vec{x})\psi_{\text{inc}}(\vec{x}), \tag{3.3}$$

where $\psi_{\text{ex}}$ is the wave at the specimen exit surface, known as the exit wave. For a thin specimen, only the phase of the incident wave is changed. For a thin and weakly interacting specimen, $t$ can be approximated as $1+\mathrm{i}\sigma v_z(\vec{x})$, where $\sigma$ is the interaction constant and $v_z$ is the projected electrostatic potential of the specimen. This is known as the weak phase object approximation (WPOA). The exit wave is focused by the objective lens. The effect of the objective lens can be described as the convolution of the exit wave with a spread function of the objective lens. Using the convolution theorem we obtain,

$$\Psi_{\text{im}}(\vec{k}) = \Psi_{\text{ex}}(\vec{k})H(\vec{k})\exp[-\mathrm{i}\chi(\vec{k})], \tag{3.4}$$

where $\Psi_{\text{im}}$ is the Fourier transform of the electron wave in the image plane, $\Psi_{\text{ex}}$ is the Fourier transform of the exit wave, and $H(\vec{k})$ is an aperture function, zero outside the aperture and one inside. $\chi$ is the aberration function from (3.2). In real space, this is

$$\begin{aligned}\psi_{\text{im}}(\vec{x}) &= (1+\mathrm{i}\sigma v_z(\vec{x})) \otimes FT^{-1}\{H(\vec{k})\exp[-\mathrm{i}\chi(\vec{k})]\} \\ &= (1+\mathrm{i}\sigma v_z(\vec{x})) \otimes \left(FT^{-1}\{H(\vec{k})\cos\chi(\vec{k})\} - FT^{-1}\{H(\vec{k})\mathrm{i}\sin\chi(\vec{k})\}\right),\end{aligned} \tag{3.5}$$

where we have set $\psi_{\text{inc}} = 1$ since it is approximately a plane wave of constant intensity. $\otimes$ represents convolution.

What is actually recorded is the intensity, $I(\vec{x}) = |\psi_{\text{im}}(\vec{x})|^2$. Hence, taking the modulus square of (3.5) and dropping the terms quadratic in $v_z$, we get $I(\vec{x}) = 1 + 2\sigma v_z(\vec{x}) \otimes FT^{-1}\{H(\vec{k}) \sin\chi\}$. The Fourier transform of the image intensity, $\tilde{I}$, is then

$$\tilde{I}(\vec{k}) \approx \delta(\vec{k}) + 2\sigma V_z(\vec{k}) H(\vec{k}) \sin\chi(\vec{k}), \tag{3.6}$$

where $\delta$ is the delta function and $V_z$ is the Fourier transform of the projected potential. This is an oscillating function for typical values of $C_s$ in a non-aberration corrected TEM. This means that different spatial frequencies will contribute differently to the image. Scherzer found that the effects of the spherical aberration can be minimized by balancing the phase shift due to $C_s$ by a suitable setting of the defocus [75], now known as Scherzer defocus. Still, the phase-contrast nature of HRTEM means that the image is quite sensitive to defocus, with no simple method of determining the correct defocus. $\sin\chi(\vec{k})$ is often called the (phase) contrast transfer function (CTF).

In practice, there will always be some degree of incoherent aberrations. If these are included, the imaging process is partially coherent. Some degree of coherence is, however, necessary in order to have phase contrast. Incoherent aberrations imply the superposition of many $\sin\chi$ that are shifted slightly with respect to each other. Hence, the CTF will be attenuated by the partial coherence at high spatial frequencies where it is oscillating rapidly. A typical CTF and the effect of partial coherence can be seen in the plot in Figure 3.4. The effect of partial coherence can be represented by envelope damping functions.

In an aberration-corrected TEM, the aberration function as it is given in (3.2) can be set to zero. From (3.6) it can be seen that this will lead to no contrast. Of course, in an aberration-corrected TEM higher-order terms must be included in the aberration function and in a real microscope this function is never zero. Still, phase contrast imaging is impossible in an aberration-free microscope. Hence, some geometrical aberrations must be introduced. It is preferable to introduce these so that the phase contrast transfer function has a broad passband, making the image easier to interpret [67]. In a $C_s$-corrected TEM this can be done by setting the defocus and $C_s$ to suitable values [77].

## 3.3 Nano-beam diffraction

Nano-beam diffraction (NBD) is a particular illumination mode that makes it possible to obtain a diffraction pattern from a very small part of the specimen. This is done by using the microscope's condenser lenses to form

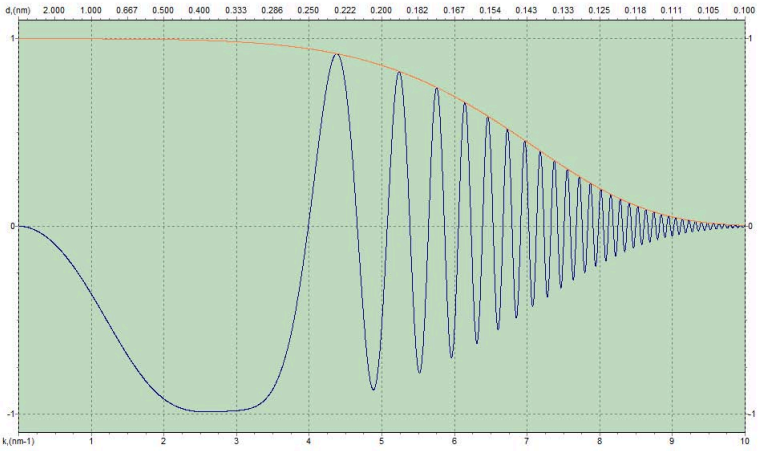


Figure 3.4: Plot of the contrast transfer function of a TEM with the following parameters: $C_s = 1.0\,\text{mm}$, defocus= $-50\,\text{nm}$ (Scherzer defocus), chromatic aberration= $1.4\,\text{mm}$, energy spread = $0.7\,\text{eV}$. The point resolution is $0.24\,\text{nm}$. The effect of the partial coherence is shown as an envelope function (orange) that dampens the oscillations of the CTF at high spatial frequencies. Made using `ctfExplorer` [76].

a small, but still approximately parallel, beam. This can be used to, for example, get a diffraction pattern from small precipitates inside an Al alloy.

## 3.4 Electron energy-loss spectroscopy

Electron energy-loss spectroscopy (EELS) measures the energy of the electrons that have gone through the specimen. This is useful because how much energy the electrons lose says something about the chemical properties of the material. The energy lost by the fast electron due to the ionization of an atom is characteristic of the atom. An EEL spectrum is a plot of intensity versus energy loss. In Paper I, EELS is used to determine the sample thickness. The proportion of inelastic scatter increases with specimen thickness. The thickness of the sample, $t$, is related to the ratio of the low-loss portion of the EEL spectrum, $I_l$, to the zero-loss peak, $I_0$, according to the formula $t = \lambda \ln I_l/I_0$ [78]. $\lambda$ is the mean free path for an electron, which in aluminium is 111 nm for electrons with an energy of 150 keV. This method of determining thickness is not very accurate and the error can be more than $\pm 10\%$ [78].

## 3.5 Convergent-beam electron diffraction

Convergent-beam electron diffraction (CBED) is a powerful technique for obtaining detailed structural information from a very small area of the specimen. Instead of using a parallel beam, the electron beam is focused into a small probe. The spots in the diffraction pattern are no longer point-like, but are discs with a width corresponding to the convergence angle of the incident beam. This means that a range of incident wave vectors impinge on the specimen in a single point, thus sampling a much larger region of reciprocal space than a selected-area diffraction pattern. The contrast inside the disc has a sensitive dependence on specimen structure factors, thickness, orientation, lattice parameters, and the electron energy.

In Paper IV in this thesis, CBED patterns are used to determine the specimen thickness in a zone axis orientation. Thickness is commonly determined using CBED in a two-beam condition, meaning the specimen is oriented such that only two beams are strongly scattered. Fringes are then visible in the CBED discs and the thickness can be determined from the spacing of these fringes [78]. This technique, although very accurate, is inconvenient in combination with STEM imaging since the STEM images must be acquired on zone. Instead, it is possible to use the fringes visible

inside the CBED discs in the zone axis orientation to match the CBED pattern to a simulated one. An accuracy of a few nanometres is possible with this method [12].

## 3.6 Scanning transmission electron microscopy

In STEM, a converged electron beam is scanned across the specimen. The transmitted and scattered electrons can then be detected by different detectors placed after the specimen. Two types of detector geometries are most commonly used, and have also been used in this thesis: bright-field (BF) detectors and high-angle annular dark-field (HAADF) detectors. A BF detector is centred on the optical axis and detects electrons that are scattered to small angles. A HAADF detector is ring shaped and therefore only detects electrons scattered to higher angles.

### 3.6.1 Forming the probe

Because the resolution of the STEM image strongly depends on the probe, the formation of the electron probe is an important topic. Generally speaking, the smaller the probe, the better the resolution will be. However, there must also be enough current in the incident beam to detect a strong enough signal at the detector. The contributions to the probe, which were mentioned above, are the condenser aperture, geometrical aberrations of the probe-forming lens, partial spatial coherence, and partial temporal coherence [67]. The size of the condenser aperture is used to set the convergence angle of the incident beam. This determines the diffraction limit for the probe size. The aberrations of the probe-forming lens limit how small the probe can be made. The spherical aberration is the most severe limitation on probe size in an uncorrected STEM.

The fact that the electron source is not a point source means that the electrons can originate from different parts of the source. The interference in the specimen plane will then not be fully coherent, due to the partial spatial coherence. The partial spatial coherence is usually stated as an effective source size. The image of the electron gun is demagnified by the condenser lenses, but a finite source is needed to provide enough current. A zero source size requires zero current.

Partial temporal coherence is the most limiting aberration in aberration-corrected microscopes for large convergence angles [67]. However, the convergence angle is typically limited so that temporal incoherence plays a negligible role.

### 3.6.2 Bright-field STEM

Placing the focused electron probe on the specimen leads to the formation of a convergent beam electron diffraction (CBED) pattern in the diffraction plane of the microscope. In conventional CBED, the convergence angle is chosen to be small enough for the diffraction discs to not overlap. In this case, the CBED pattern is independent of probe position and also unaffected by lens aberrations [79]. However, in STEM, the CBED discs do overlap. In this case, different diffracted beams will interfere with one another in the overlap region. The approach of Nellist and Pennycook [5] allows bright-field and high-angle annular dark-field STEM to be treated within the same framework. Following [5], the probe is written in reciprocal space as an aperture function $A(\vec{k}_i) = H(\vec{k}_i)\exp[-\mathrm{i}\chi(\vec{k}_i)]$, where $\vec{k}_i$ is an incident transverse wave vector. The real-space probe wave function, $P(\vec{x})$, is the inverse Fourier transform of $A$:

$$P(\vec{x}) = \int A(\vec{k}_i)\exp[\mathrm{i}2\pi\vec{k}_i\cdot\vec{x}]\,\mathrm{d}\vec{k}_i \tag{3.7}$$

A change in probe position in the specimen plane corresponds to a phase shift in reciprocal space, this can therefore be included as a phase multiplier:

$$A(\vec{k}_i) \rightarrow A(\vec{k}_i)\exp[-\mathrm{i}2\pi\vec{k}_i\cdot\vec{x}_0], \tag{3.8}$$

where $\vec{x}_0$ is the probe position. For a thin specimen, the scattering of the incident transverse wave vector, $\vec{k}_i$, into a final transverse wave vector, $\vec{k}_f$, can be described by the complex multiplier $\Psi(\vec{k}_f, \vec{k}_i)$. The intensity in the detector plane can then be written as

$$I(\vec{k}_f, \vec{x}_0) = \left|\int A(\vec{k}_i)\exp[-\mathrm{i}2\pi\vec{k}_i\cdot\vec{x}_0]\Psi(\vec{k}_f,\vec{k}_i)\,\mathrm{d}\vec{k}_i\right|^2. \tag{3.9}$$

Expanding the square and some further manipulation yields the intensity in terms of reciprocal space variables:

$$\tilde{I}(\vec{k}_f, \vec{q}) = \int A(\vec{k}_i)A^*(\vec{k}_i+\vec{q})\Psi(\vec{k}_f,\vec{k}_i)\Psi^*(\vec{k}_f,\vec{k}_i+\vec{q}). \tag{3.10}$$

This equation can be interpreted as follows: Two incident partial plane waves $\vec{k}_i$ and $\vec{k}_i+\vec{q}$ are scattered by the specimen into the same final wave vector $\vec{k}_f$ in the detector plane (see Figure 3.5). There, they interfere and contribute to the image spatial frequency $\vec{q}$. This can only happen in disc overlap regions in the CBED pattern. The phase difference between $\vec{k}_i$ and $\vec{k}_i + \vec{q}$ will be $2\pi\vec{q}\cdot\vec{x}_0$. As the probe is scanned, changing $\vec{x}_0$, $\vec{k}_i$ and $\vec{k}_i + \vec{q}$ will always interfere at $\vec{k}_f$, but since the phase difference changes the intensity will

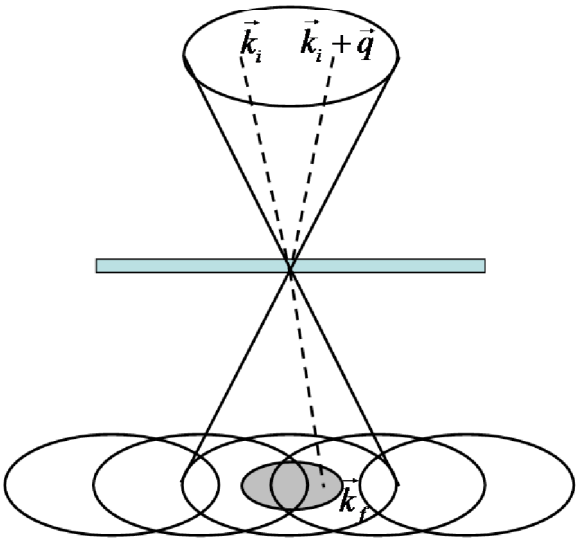


Figure 3.5: Schematic drawing illustrating image formation in bright-field STEM. Because of the overlap of the discs, both incident wave vectors $\vec{k}_i$ and $\vec{k}_i + \vec{q}$ are scattered by the specimen into the same final wave vector $\vec{k}_f$ in the detector plane, where they interfere. The phase difference between the two incident wave vectors depends on probe position. The intensity in the detector plane will therefore oscillate as the probe is scanned.

oscillate at a rate determined by $\vec{q}$. By placing a detector in the diffraction plane, an image can be formed. In bright-field STEM, placing the detector on the optical axis allows the interference between the central, undiffracted, disc and the diffracted discs to be used. A point detector would give perfect coherence. In practice, a finite detector must be used, which leads to a reduction in the coherence [79]. To keep a sufficient degree of the coherence, the bright-field detector should be smaller than the convergence angle of the probe.

Bright-field STEM can also be understood using the theorem of reciprocity. This theorem states that, in the case of elastic scattering, the signal detected at point A originating from a source at point B, has the same amplitude and phase as would be detected at point B if the source were placed at point A [73]. For small energy losses the intensity is conserved, and not the amplitude and phase. This principle implies that a certain illumination geometry in TEM, corresponds to a certain detector geometry in STEM. Specifically, parallel illumination in TEM corresponds to a point detector

placed on the optical axis in STEM. A large detector in STEM corresponds to illumination over a range of angles in TEM. Similarly, a finite source size in STEM is equivalent to a finite pixel size in TEM.

### 3.6.3 HAADF STEM

A simple way of understanding intensity in a HAADF image, is to realize that heavy atoms scatter more strongly to higher angles, and that the incident electrons are attracted to the positive nucleus of the atoms. This means that when the probe is positioned on a column of heavy atoms, more electrons will be scattered to high angles where the detector is located, than if the probe is positioned between atomic columns or on light atomic columns. Also, a probe positioned on a heavy column will not disperse as quickly as a probe placed elsewhere, because of the attraction to the nucleus. This is known as channeling [71].

Because of the reliance on interference between overlapping discs, BF STEM is a coherent imaging mode, just like HRTEM. HAADF STEM, on the other hand, can be considered to be an incoherent imaging mode. The simplest model of HAADF imaging, the object function model [80], states that the image intensity is simply the convolution of the probe wave function with an object function representing the specimen:

$$I(x) = |P(x)|^2 \otimes O(x). \tag{3.11}$$

$|P(x)|^2$ is known as the point-spread function, since it smears a point in the specimen into a disc in the image. (3.11) is the definition of incoherent imaging [5]. Incoherent imaging requires that rays emerging from different parts of the specimen do not have a fixed phase relationship.

There are two main causes for the incoherent nature of HAADF imaging: the large size of the HAADF detector and thermal diffuse scattering (TDS). Following [5], we will first consider the effect of the detector. We still assume a thin specimen, so that the effect of the specimen on the wave function is described by multiplication with a specimen function, $\Psi$, in reciprocal space. Starting with (3.10), we integrate this intensity in the detector plane over a detector function $D(\vec{k}_f)$:

$$\begin{aligned}\tilde{I}(\vec{q}) = &\int A(\vec{k}_i - \vec{q}/2)A^*(\vec{k}_i + \vec{q}/2) \\ &\times \int D(\vec{k}_f)\Psi(\vec{k}_f - \vec{k}_i + \vec{q}/2)\Psi^*(\vec{k}_f - \vec{k}_i - \vec{q}/2)\,\mathrm{d}\vec{k}_f\mathrm{d}\vec{k}_i.\end{aligned} \tag{3.12}$$

$D(\vec{k}_f)$ is equal to one where the detector is, and zero elsewhere. Now if the detector is large, the dependence of the second integral on $\vec{k}_i$ is small. This

allows the two integrals to be separated:

$$\begin{aligned}\tilde{I}_{\mathrm{HAADF}}(\vec{q}) &= \int A(\vec{k}_i - \vec{q}/2)A^*(\vec{k}_i + \vec{q}/2)\,\mathrm{d}\vec{k}_i \\ &\quad \times \int D(\vec{k}_f)\Psi(\vec{k}_f - \vec{k}_i + \vec{q}/2)\Psi^*(\vec{k}_f - \vec{k}_i - \vec{q}/2)\,\mathrm{d}\vec{k}_f \\ &= T(\vec{q})\tilde{O}(\vec{q}).\end{aligned} \tag{3.13}$$

Taking the inverse Fourier transform of this yields in real space:

$$I_{\mathrm{HAADF}}(\vec{x}_0) = |P(\vec{x}_0)|^2 \otimes O(\vec{x}_0), \tag{3.14}$$

which is exactly the definition of incoherent imaging given in (3.11).

Hence, a large detector relative to the overlap between discs separated by the reciprocal space vector $\vec{q}$, allows the integral in (3.12) to be separated. Put another way, the large detector implies an integration over many final wave vectors, $\vec{k}_f$, thus destroying the coherence. One might think this should also lead to a reduction in contrast. However, the image contrast can be maintained by a hole in the detector, as will be discussed next.

Contrast in the incoherent HAADF image is provided by the hole in the detector [81]. To understand the effect of the detector, we must consider the object function, $\tilde{O}(\vec{q})$ in (3.13). The inverse Fourier transform of the detector with a hole is, just as for an aperture, an Airy function in real space. Nellist and Pennycook show that the object function will be non-zero only if the projected potential varies over a length scale of the order of the central maximum of the Airy disc [5]. Thus, the detector hole gives rise to a coherence envelope, within which interference between different parts of the specimen is allowed. For suitable detector geometries the coherence envelope is narrow enough to prevent interference between wave vectors scattered from different atomic columns, but large enough to allow interference within a column.

For thicker specimens, dynamical scattering must be taken into account. In this case, the effect of the detector can be analysed by using the Bloch wave formulation of dynamical scattering. It is found that the detector hole acts as a kind of Bloch state filter [5], allowing only the highly localized Bloch states to contribute to the image. These are the so-called 1$s$-type states that are localized on the atomic columns.

While the large size of the HAADF detector causes the scattering from different atomic columns to be incoherent, it does not prevent interference within a column. In other words, the detector provides good transverse incoherence but poor incoherence parallel to the beam. Instead, the longitudinal

incoherence is provided by TDS. Many of the electrons scattered to high angles will have been scattered by phonons. This is known as thermal diffuse scattering, or TDS. TDS is an inelastic scattering process, but typically only very little of the electron's energy is lost, roughly 0.1 eV. TDS results in a redistribution of electrons scattered to high angles from the Bragg beams into a diffuse background. TDS will cause incoherence, partly because the scattering is inelastic, but also because phonons impart extra momentum to the electrons. Just like a large detector led to transverse incoherence by integrating over many final transverse wave vectors, $\vec{k}_f$, TDS will lead to a summation over many final wave vectors with different vertical components, leading to longitudinal incoherence.

### 3.6.4 Simulating HAADF STEM images

Simulating TEM or STEM images or diffraction patterns requires an accurate calculation of how the incident electron wave is affected by the specimen. This requires taking into account the effects of dynamical diffraction. There are two methods commonly used: the Bloch wave method and the multislice method [74]. In the Bloch wave method, the electron wave and the specimen potential are both expressed in a basis set having the periodicity of the specimen, the Bloch states. The Schrödinger equation is then solved, determining the beams leaving the specimen at the exit surface [82].

The most common method of simulating STEM images is known as multislice [83]. In this approach, the specimen is divided into many slices that are perpendicular to the incident beam and 1–2 Å thick. The projected crystal potential for each slice is then calculated. The scattering of the incident electrons by each slice is divided into two steps: transmission by the projected crystal potential, and propagation through vacuum to the next slice, as shown in Figure 3.6. This process is then reiterated for each slice, until the exit surface of the specimen. Mathematically this can be expressed by the equation [74]:

$$\psi_{n+1}(x,y) = p_n(x,y,\Delta z_n) \otimes [t_n(x,y)\psi_n(x,y)], \tag{3.15}$$

where $\psi_n$ is the wave function before slice $n$, $p_n$ is the propagator for slice $n$, and $t_n$ is the transmission function for slice $n$. $\Delta z_n$ is the slice thickness, which is typically the same for each slice. The propagator is determined using Fresnel diffraction, and is most easily expressed in reciprocal space, as $P_n(k_x, k_y, \Delta z_n)$. Through the convolution theorem, (3.15) can be restated using Fourier transforms:

$$\psi_{n+1}(x,y) = \mathrm{FT}^{-1}\{P_n(k_x,k_y,\Delta z_n)\mathrm{FT}[t_n(x,y)\psi_n(x,y)]\}. \tag{3.16}$$

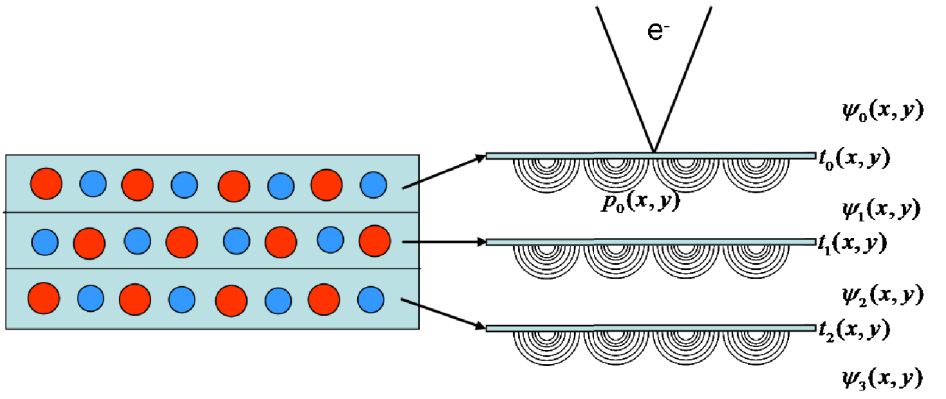


Figure 3.6: Schematic drawing illustrating the multislice method of simulating the beam-specimen interaction. The crystal, shown on the left, is divided into many thin slices, shown on the right.

The multislice method therefore involves the calculations of many Fourier transforms. This can be readily implemented on a computer using the fast Fourier transform (FFT). The multislice program `stemimg` written by C. Dwyer [84], based on the code developed by E. J. Kirkland [74], was used in Paper II and Paper IV.

As a result of the discrete nature of the FFT, the supercell is repeated indefinitely in the plane. Hence, the left side of the supercell is touching the right side of the supercell, and the same for the top and the bottom. This has two important consequences when trying to avoid artefacts. Firstly, the periodicity of the supercell should match the periodicity of the specimen, i.e., the supercell should consist of a whole number of unit cells. Secondly, the transmission functions and the wave functions must not be allowed to overlap with these functions in neighbouring supercells. The solution to this problem is to set these functions to zero beyond a certain spatial frequency where the overlap takes place. This is known as bandwidth limiting [74]. In practice, the maximum spatial frequency is set to 2/3 of the maximum sampling frequency.

The effects of thermal diffuse scattering were not included in the first multislice programs. TDS can be included in the calculation using the frozen phonon technique [85]. Because the velocity of the electrons is much higher than the frequency of the oscillations of the atoms, the incident electrons essentially see a "frozen" atomic lattice. This can be included in the multislice calculation by displacing the atoms randomly from their equilibrium

positions, the amplitude of the displacement determined by the temperature factor. The temperature factor is a measure of the amplitude of the vibrations of an atom. The frozen phonon technique requires the averaging over many different frozen phonon configurations. A benefit of the frozen phonon technique is that, although it increases the time required for a simulation, effects such as multiple phonon scattering and the subsequent elastic scattering of a phonon-scattered electron are included. In the alternative method of including inelastic scattering, using an absorptive potential, these events are not included [86].

STEM multislice simulations are therefore more time consuming than HRTEM simulations. A separate multislice calculation is required for each probe position, or pixel, in the STEM image. Also, several different phonon configurations must calculated and averaged over. In a typical crystalline specimen a slice is repeated several times through the thickness of the specimen. In a HRTEM simulation, time is saved by reusing the same projected potentials through the thickness of the specimens, if the specimen is periodic in the beam direction. In HAADF STEM however, it is better to calculate a different projected potential each time a slice is used, with different random displacements due to thermal vibrations. Recently, STEM multislice calculations have seen a considerable decrease in computation time by making use of the parallelization possible on graphical processing units [84].

The effects of the condenser aperture and the aberrations in the probe-forming lens are included in the multislice calculation when forming the incident wave function, $\psi_0$. The temporal incoherence can be included in the simulation as a spread in defocus. This involves running the simulation for different defocuses and adding the different runs together, weighting each run according to a Gaussian distribution. Temporal incoherence typically only has a small effect compared to the spatial incoherence and can therefore be ignored [87]. Spatial incoherence can be included in the image after the multislice calculation has been completed, by convolving the image with the effective source [81]. The source is normally expressed as a Gaussian distribution with a certain full-width at half maximum (FWHM).

By its nature, performing simulations on a computer requires a discrete sampling of the quantities involved: the electron wave function, the specimen transmission function for each slice, and the propagator for each slice. It is important to make sure that the sampling is sufficient to avoid artefacts in the simulation. First of all, the wave functions must be adequately sampled. The slice thickness should ideally include one layer of atoms, leading to a slice thickness of 1–2 Å. In the lateral dimensions the slices and the wave function have a real space size of $a \times b$, referred to as the supercell. This

supercell is sampled by $N_x \times N_y$ pixels, leading to a pixel size of $\Delta x = a/N_x$ and $\Delta y = b/N_y$, as shown in Figure 3.7. The pixels do not have to be square. In reciprocal space, the reciprocal pixel sizes are $\Delta k_x = 1/a$ and $\Delta k_y = 1/b$. Adequate sampling requires that [74]:

- The pixel size is less than a quarter of the resolution required in the final image.
- The reciprocal space pixel size is less than $k_{\text{conv}}/10$, where $k_{\text{conv}}$ is the size of the convergence semi-angle in reciprocal space units. The reciprocal space pixel size is reduced by increasing the size of the supercell.
- The reciprocal space is sampled out to the outer angle of the STEM detector. The maximum sampling frequency is $N_x/(2a)$, the Nyquist frequency. However, bandwidth limiting requires that the outermost third of spatial frequencies is set to zero. Hence, the maximum spatial frequency is $N_x/(3a)$, which must be greater than the outer angle of the detector. If the pixels are not square, the maximum spatial frequency will be different in the $x$- and $y$-directions. To avoid artefacts, the maximum spatial frequency should be set to the minimum of the two directions.

In addition, the supercell should be large enough to avoid overlap of the wave function between neighbouring supercells due to the wave function spreading out as it passes through the specimen. This issue is separate from the one of bandwidth limiting described above. A thicker specimen requires a larger supercell. A lower limit on the thickness, $t$, for which there is no overlap is given by the formula $t = a/(2\alpha)$, where $\alpha$ is the convergence semi-angle. It is a lower limit since channeling of the probe will normally keep it from spreading out as much as in the case of no specimen.

Finally, there is also the question of how many probe positions are required. The computation time increases linearly with the number of probe positions. Reducing the number of probe positions is therefore desirable. Firstly, only the smallest repeating unit of the supercell needs to be sampled. Secondly, the minimum number of probe positions required in each scan direction is determined by the information limit. Using the diffraction limit (determined by the convergence angle) as the information limit, the number of required probe positions in each scan direction is given by $4ak_{\text{conv}}$, rounded up to the nearest integer [84]. $a$ is here the length of one dimension of the scanned area, and $k_{\text{conv}}$ is the highest spatial frequency passed by the condenser aperture. Using more probe positions than this does not

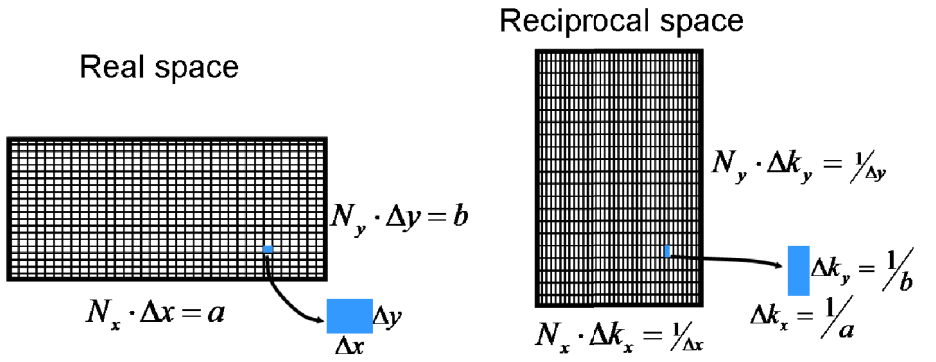


(a) Real space (b) Reciprocal space

Figure 3.7: Each horizontal slice is sampled by a finite number of pixels in real and reciprocal space. A small pixel size in reciprocal space requires a large supercell in real space.

increase the amount of information in the image. To make the pixelation less visible and make the image more aesthetically pleasing, the image can instead be interpolated. A suitable interpolation method is to surround the Fourier transform of the image with pixels having zero intensity (known as zero-padding) [84]. Inverse Fourier transforming the resulting image gives a much smoother image.

The processing applied to the output from the simulation program is illustrated in Figure 3.8, where aluminium is used as an example. The raw simulation output is first interpolated, and then convoluted with a two-dimensional Gaussian function corresponding to the probe.

### 3.6.5 Quantitative HAADF STEM

HAADF STEM is a fairly robust imaging method. There are no contrast reversals with a change in thickness or defocus. This makes it possible to extract quantitative information from HAADF STEM images under certain conditions. This has been done in Paper IV. Because of the dynamical nature of electron scattering, quantitative HAADF STEM requires the comparison between experimental and simulated images. In this respect, HAADF STEM is similar to HRTEM. However, while in HRTEM the specimen thickness and defocus is varied for a trial structure, in HAADF STEM, the incoherent nature of the image allows for an easier determination of the projected

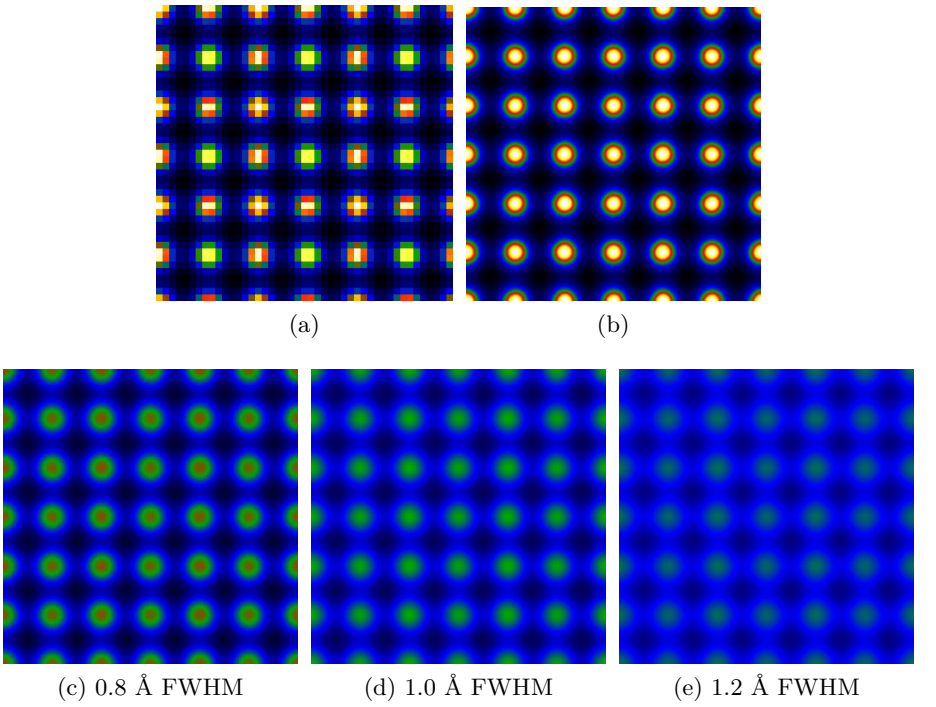

(a) (b)

(c) 0.8 Å FWHM (d) 1.0 Å FWHM (e) 1.2 Å FWHM

Figure 3.8: Simulated image of Al (3x3 unit cells) showing (a) the raw image, (b) the image after interpolation, (c–e) the image in (b) after convolution with a Gaussian probe with a FWHM as indicated. All the images have the same intensity levels (min = 0.012, max = 0.07). Simulation parameters: sample thickness: 603.45 Å, probe convergence semi-angle: 18 mrad, HAADF detector angles: 59–200 mrad, no geometrical aberrations.

structure. Thus, simulations for different thicknesses and chemical compositions can be performed instead. If the thickness is determined through some other means, the composition can be determined.

Direct comparison between experimental and simulated HAADF STEM images requires, first of all, the characterization of the HAADF detector response. In a typical STEM simulation, the incident probe intensity is normalized to one. The simulated image intensity is therefore a number between 0 and 1, inclusive. The intensity of the experimental image, however, depends on the offset and gain settings (corresponding to brightness and contrast, respectively) of the amplifier connected to the HAADF detector. The offset can be determined by measuring the intensity on the detector when the probe is not on the specimen, $I_{\text{vac}}$ (corresponding to a normalized intensity of 0). To determine the gain, the easiest method is to scan the probe across the detector, obtaining an image of the detector (Figure 3.9). This gives the intensity corresponding to a normalized intensity of 1, $I_{\text{det}}$. This also makes it possible to observe any non-uniformities in the detector response. Placing the probe on the detector is done by leaving diffraction mode while in STEM mode, causing an image of the focused probe to be formed in the detector plane. The intensity in the experimental image, $I_{\text{raw}}$, can then be normalized to yield normalized intensites $I_{\text{norm}}$ using the formula [11]

$$I_{\text{norm}} = \frac{I_{\text{raw}} - I_{\text{vac}}}{I_{\text{det}} - I_{\text{vac}}}. \tag{3.17}$$

This was first demonstrated by LeBeau et al. [88, 89], who used their own amplifier. It has later become common to use the hardware supplied by the manufacturer.

Once the experimental image has been normalized, direct comparison with simulated images is possible. The image intensities will of course depend on thickness. It is therefore preferable to determine the thickness through separate means. Two methods are used in the literature: EELS and CBED. When using CBED, the structure inside the discs in the experimental pattern is compared qualitatively with simulated patterns of different thicknesses. The advantage of CBED is that only the crystalline parts of the specimen will contribute to the structure inside the discs; amorphous layers at the entrance or exit surface of the specimen do not contribute. The probe is scanned over an area several unit cells large, as suggested by LeBeau et al. [90]. This removes any coherent effects from the CBED pattern recorded by the CCD camera. However, in Paper IV, the convergence angle was reduced when acquiring the CBED pattern by switching to a smaller aperture, reducing the amount of overlap between the CBED discs. This

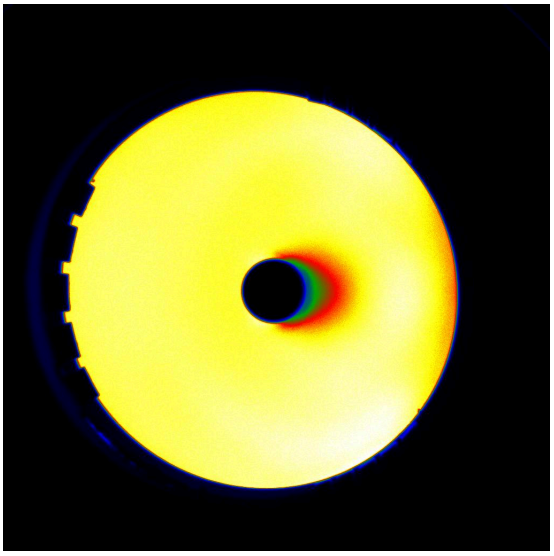

Figure 3.9: An image of the HAADF detector on the FEI Titan$^3$ 80-300 at Monash University. The image is formed by scanning a focused probe across the detector.

leads to more detail in the CBED discs and hence facilitates the matching of experimental and simulated CBED patterns.

To actually compare simulated and experimental intensities, different approaches are possible. The simplest method is to compare the average intensity inside a projected unit cell of the crystal. This is the simplest method since the average unit cell intensity is independent of the effective source size, since the source size only smears out the intensity, leaving the average intensity unchanged. If instead intensities inside the unit cell are compared, such as column intensities, the effective source size must be determined. In the case of Al alloys, the aluminium matrix can be used to determine the effective source size. Once this has been done, the intensities of individual atomic columns in the experimental and the simulated images can be compared. Alternatively, suitably chosen line profiles can be used. Line profiles have the advantage that both the intensity maxima and the background are compared.

## 3.7 Quantification of alloy microstructure using TEM

The microstructure of the two alloys introduced in Paper I was quantified using the methodology discussed by Marioara et al. [91] and Andersen [92]. The precipitate needle lengths and cross-section sizes are measured from BF TEM images acquired in a $\langle 001 \rangle_{\mathrm{Al}}$ zone axis. The precipitate needles grow along all three $\langle 001 \rangle_{\mathrm{Al}}$ directions. The number of precipitates oriented parallel to the beam in an image is counted and the process repeated for several images. To get the precipitate number density, the thickness, $t$, of the sample must be known. This value is measured using EELS. The precipitate volume fraction (i.e., the fraction of the grain consisting of precipitates) is then the number density of the precipitates, $\rho$, multiplied by the average needle length, $\lambda$, and the average cross-section size.

However, in measuring the precipitate number density and the average needle length, the effect of needles being cut in sample preparation must be taken into account. To account for needles whose original centre lies outside the specimen, the thickness used for the number density calculation is an effective thickness that is the sum of the measured thickness and the average needle length. The number density then becomes

$$\rho = \frac{3N}{A\,(t + \lambda)}, \tag{3.18}$$

where N is the number of needles oriented parallel to the beam in an area, $A$. The factor of 3 stems from there being three equivalent $\langle 001 \rangle_{\mathrm{Al}}$ directions and only precipitates parallel to the beam are counted.

If the foil normal is not parallel to the incident beam, some of the precipitate needles that are used in calculating the average needle length will likely have been cut in the specimen preparation process. The actual average needle length, $\lambda$, can be approximated using the equation [92]

$$\lambda = \frac{l_m}{1 - \frac{l_m}{t} \cos\theta \tan\phi}, \tag{3.19}$$

where $l_m$ is the average needle length as measured, $\phi$ is the angle formed by the foil normal and the zone axis, and $\theta$ describes the orientation of the needles perpendicular to the beam with respect to the specimen surface. $\theta$ is zero when one of the two $\langle 001 \rangle_{\mathrm{Al}}$ directions perpendicular to the incident beam is parallel to the foil surfaces. $\theta$ is typically not known, but using $\theta = 45°$ gives reasonably accurate results [92].

# Chapter 4

# Conclusions and outlook

The main conclusions from each of the four papers contained in this thesis can be summarized as follows:

**Paper I** Two different Al-Mg-Ge alloys were investigated, one Mg-rich and one Ge-rich. No $\beta''$ was observed near peak hardness. Instead, U1-Ge and $\beta'$-Ge precipitates as well as disordered precipitates were present. The hexagonal Ge network could be directly imaged using HAADF STEM and was present in all the precipitates. The $U1$-Ge and $\beta'$-Ge precipitates are finer and have different orientation relationships from what is common in Al-Mg-Si alloys.

**Paper II** The Ge-rich alloy in Paper I was investigated using aberration-corrected HAADF STEM. The $U1$-Ge precipitates were found to have an interesting interface structure, with Ge-rich columns decorating the interface. The disordered precipitates could often be divided into building blocks that were related to each other through a two-fold rotation.

**Paper III** Precipitation in an Al-Mg-Si-Ge-Cu alloy was studied using aberration-corrected HAADF STEM. This alloy was similar to the Mg-rich alloy in Paper I, but half of the Ge was replaced with Si and 0.13 at. % Cu added. The precipitates were often lath-shaped, similar to the $L$ phase in Al-Mg-Si-Cu alloys. No repeating unit cell was observed, but the hexagonal Si/Ge network was present in all the precipitates. Cu columns appeared in the same atomic arrangement as seen in Al-Mg-Si-Cu alloys. The Cu-free parts of the precipitates consisted of structural units with Mg and Al at specific sites. These structural units were often arranged in an ordered fashion.

**Paper IV** The $\beta'$-Ge precipitates in the Mg-rich alloy in Paper I were investigated using quantitative aberration-corrected HAADF STEM. The image intensities were normalized with respect to the incident beam, allowing direct comparison between experiment and simulation. The Ge-rich columns were found to be only partially occupied by Ge. A partial replacement of Ge by Al or vacancies could explain the smaller lattice parameter of $\beta'$-Ge observed in this alloy compared with coarser $\beta'$-Ge precipitates and $\beta'$ in Al-Mg-Si alloys. The $\beta'$-Ge precipitates were also observed to have an interesting interface structure, with a Ge-containing matrix column occurring periodically along the coherent interface when viewed along the needle direction.

## 4.1 Conclusions and outlook: 6xxx and related alloys

Al-Mg-Ge alloys do not appear to have vastly improved properties over Al-Mg-Si. Ge is also considerably more expensive than Si. Industrial applications are therefore limited, although trace additions of Ge have been investigated [63], and are an interesting possibility. Studying an alloy very similar to, but different from, Al-Mg-Si has given new clues to understanding precipitation in 6xxx alloys. Also, the higher atomic number of Ge made it straightforward to determine the Ge-rich columns using HAADF STEM.

One of the questions this thesis has raised is whether observations made in the Al-Mg-Ge system also apply to Al-Mg-Si(-Cu) precipitates. For example, do the structural units found in the Al-Mg-Si-Ge-Cu alloy in Paper III also exist in Al-Mg-Si-Cu precipitates, such as the $L$ phase? In other words, is there a local order in addition to the Si network? Also, interesting ordered interfaces have been observed in $U1$-Ge, $\beta'$-Ge, and some disordered precipitates. This might be described as an ordered intermixing at the interface. Do similar interface structures exist in Al-Mg-Si(-Cu) alloys?

The analysis in this thesis of the precipitate/matrix interfaces has been somewhat simplistic. It might be beneficial to describe these interfaces within the framework of an interface theory [93, 94]. There are few studies of precipitate/matrix interfaces in the literature, perhaps due to the fact that they were difficult to study on an atomic scale before the advent of aberration correctors.

Although attempts were made, first-principles atomistic calculations using density functional theory (DFT) were not included in this thesis. It would be useful to test some of the conclusions drawn from experimental observations using DFT, for example the interface structures of $U1$-Ge and

$\beta'$-Ge, and the structural units observed in Al-Mg-Si-Ge-Cu. It would also be interesting, although difficult, to determine the actual structure of $\beta'$-Ge.

## 4.2 Conclusions and outlook: HAADF STEM

To answer some of the questions raised in the previous section, advanced TEM techniques will be necessary. HAADF STEM is a powerful imaging method that is particularly suited for studying precipitates. The incoherent nature of the images allows bright dots to be interpreted as atomic columns, while the atomic-number dependence provides chemical information. It appears to be replacing exit-wave reconstruction from HRTEM images, although HAADF STEM is not suitable for imaging very light atoms (e.g., Li).

Quantitative HAADF STEM can be a useful method in structure determination of small crystals such as precipitates. For small particles and near interfaces other quantitative methods such as quantitative electron diffraction and EDXS are not as useful because of the larger probe size needed. HAADF STEM and TEM are often used to form an initial structural model. HAADF STEM has the advantage that structural and compositional information can be gained from a single image.

A drawback of quantitative HAADF STEM is the need for simulations. This requires an accurate knowledge of the microscope parameters and the crystal structure. The process of comparing experimental and simulated images is somewhat tedious and appropriate computer programs could make it more user friendly. Different ways of doing the comparison are used in the literature and establishing a standard method might benefit the STEM community. The accuracy of the method when used on precipitates could be investigated by using it on known phases in the Al-Mg-Si(-Cu) system. A challenge in Al-Mg-Si alloys is the difficulty in distinguishing between Mg, Al, and Si. It appears that this is sometimes possible although caution is needed. The situation is helped by the variation in the temperature factor, which for these three elements decreases with atomic number [95]. Thus, the fact that Mg columns often appear as dimmer spots is due to both the lower atomic number and the higher temperature factor typical of alkali and alkaline earth metals. There is no doubt that the application of HAADF STEM to studies of 6xxx and other alloy systems has a bright future.

# References


[1] I. J. Polmear. Aluminium alloys - a century of age hardening. *Materials Forum*, 28, 2004.

[2] S. J. Andersen, C. D. Marioara, R. Vissers, A. Frøseth, and H. W. Zandbergen. The structural relation between precipitates in Al-Mg-Si alloys, the Al-matrix and diamond silicon, with emphasis on the trigonal phase U1-$MgAl_2Si_2$. *Materials Science and Engineering: A*, 444(1-2):157–169, 2007.

[3] C. D. Marioara, S. J. Andersen, T. N. Stene, H. Hasting, J. Walmsley, A. T. J. van Helvoort, and R. Holmestad. The effect of Cu on precipitation in Al-Mg-Si alloys. *Philosophical Magazine*, 87(23):3385–3413, 2007.

[4] S. J. Pennycook and D. E. Jesson. High-resolution incoherent imaging of crystals. *Physical Review Letters*, 64(8):938, 1990.

[5] P. D. Nellist and S. J. Pennycook. The principles and interpretation of annular dark-field Z-contrast imaging. In *Advances in Imaging and Electron Physics*, volume 113 of *Advances in Imaging and Electron Physics*, pages 147–203. Academic Press Inc, San Diego, 2000.

[6] Y. Mishin, M. Asta, and J. Li. Atomistic modeling of interfaces and their impact on microstructure and properties. *Acta Materialia*, 58(4):1117–1151, 2010.

[7] Y. Wang, Z. K. Liu, L. Q. Chen, and C. Wolverton. First-principles calculations of $\beta''$-$Mg_5Si_6$/$\alpha$-Al interfaces. *Acta Materialia*, 55(17):5934–5947, 2007.

[8] S. Y. Hu, M. I. Baskes, M. Stan, and L. Q. Chen. Atomistic calculations of interfacial energies, nucleus shape and size of $\theta'$ precipitates in Al-Cu alloys. *Acta Materialia*, 54(18):4699–4707, 2006.

[9] M. Torsæter, F. J. H. Ehlers, C. D. Marioara, S. J. Andersen, and R. Holmestad. Applying precipitate-host lattice coherency for compositional determination of precipitates in Al-Mg-Si-Cu alloys. *Submitted to Philosophical Magazine*, 2011.

[10] K. Kuramochi, K. Suzuki, T. Yamazaki, K. Mitsuishi, K. Furuya, I. Hashimoto, and K. Watanabe. Quantitative structural analysis of twin boundary in $\alpha$-$Zn_7Sb_2O_{12}$ using HAADF STEM method. *Ultramicroscopy*, 109(1):96–103, 2008.

[11] A. Rosenauer, K. Gries, K. Müller, A. Pretorius, M. Schowalter, A. Avramescu, K. Engl, and S. Lutgen. Measurement of specimen thickness and composition in $Al_xGa_{1-x}N$/GaN using high-angle annular dark field images. *Ultramicroscopy*, 109(9):1171–1182, 2009.

[12] C. Dwyer, M. Weyland, L. Y. Chang, and B. C. Muddle. Combined electron beam imaging and ab initio modeling of $T_1$ precipitates in Al–Li–Cu alloys. *Applied Physics Letters*, 98(20):201909–3, 2011.

[13] S. Venetski. Silver from clay. *Metallurgist*, 13(7):451–453, 1969.

[14] J. D. Verhoeven. *Fundamentals of physical metallurgy*. Wiley, New York, 1975.

[15] E. O. Hall. The deformation and ageing of mild steel: III discussion of results. *Proceedings of the Physical Society. Section B*, 64(9):747, 1951.

[16] N. J. Petch. The cleavage strength of polycrystals. *Journal Iron Steel Inst.*, 174:25–28, 1953.

[17] A. Wilm. Physikalisch-metallurgische untersuchungen über magnesiumhaltige aluminiumlegierungen. *Metallurgie*, 8:225–227, 1911.

[18] P. D. Merica, R. G. Waltenberg, and H. Scott. Heat treatment of duralumin. *Bull. Am. Inst. Min. Metall. Eng.*, 150:913–949, 1919.

[19] S. Coriell. Precipitation hardening of metal alloys. In D. R. Lide, editor, *A century of excellence in measurements, standards, and technology*, pages 14–15. NIST, 2001.

[20] A. Guinier. A new type of x-ray diagram. *Comptes rendus de l'Académie des sciences*, 206:1641, 1938.

[21] G. D. Preston. Structure of age-hardened aluminium-copper alloys. *Nature*, 142:570, 1938.

[22] D. A. Porter and K. E. Easterling. *Phase transformations in metals and alloys*. Stanley Thornes, Cheltenham, 2000.

[23] M. A. van Huis, J. H. Chen, M. H. F. Sluiter, and H. W. Zandbergen. Phase stability and structural features of matrix-embedded hardening precipitates in Al-Mg-Si alloys in the early stages of evolution. *Acta Materialia*, 55(6):2183–2199, 2007.

[24] E. Hornbogen. Hundred years of precipitation hardening. *Journal of Light Metals*, 1(2):127–132, 2001.

[25] J. E. Hatch. *Aluminum: properties and physical metallurgy*. Aluminum Association, 1984.

[26] M. H. Jacobs. The structure of the metastable precipitates formed during ageing of an Al-Mg-Si alloy. *Philosophical Magazine*, 26(1):1–13, 1972.

[27] G. A. Edwards, K. Stiller, G. L. Dunlop, and M. J. Couper. The precipitation sequence in Al-Mg-Si alloys. *Acta Materialia*, 46(11):3893–3904, 1998.

[28] R. Vissers, M. A. van Huis, J. Jansen, H. W. Zandbergen, C. D. Marioara, and S. J. Andersen. The crystal structure of the $\beta'$ phase in Al-Mg-Si alloys. *Acta Materialia*, 55(11):3815–3823, 2007.

[29] W. F. Smith. Effect of reversion treatments on precipitation mechanisms in an Al-1.35 at pct $Mg_2Si$ alloy. *Metallurgical Transactions*, 4(10):2435–2440, 1973.

[30] C. D. Marioara, S. J. Andersen, J. Jansen, and H. W. Zandbergen. Atomic model for GP-zones in a 6082 Al-Mg-Si system. *Acta Materialia*, 49(2):321–328, 2001.

[31] K. Matsuda, H. Gamada, K. Fujii, Y. Uetani, T. Sato, A. Kamio, and S. Ikeno. High-resolution electron microscopy on the structure of Guinier-Preston zones in an Al-1.6 mass pct $Mg_2Si$ alloy. *Metallurgical and Materials Transactions a-Physical Metallurgy and Materials Science*, 29(4):1161–1167, 1998.

[32] S. J. Andersen, H. W. Zandbergen, J. Jansen, C. Træholt, U. Tundal, and O. Reiso. The crystal structure of the $\beta''$ phase in Al-Mg-Si alloys. *Acta Materialia*, 46(9):3283–3298, 1998.

[33] H. S. Hasting, A. G. Frøseth, S. J. Andersen, R. Vissers, J. C. Walmsley, C. D. Marioara, F. Danoix, W. Lefebvre, and R. Holmestad. Composition of $\beta''$ precipitates in Al–Mg–Si alloys by atom probe tomography and first principles calculations. *Journal of Applied Physics*, 106(12):123527–9, 2009.

[34] C. D. Marioara, S. J. Andersen, J. Jansen, and H. W. Zandbergen. The influence of temperature and storage time at RT on nucleation of the $\beta''$ phase in a 6082 Al-Mg-Si alloy. *Acta Materialia*, 51(3):789–796, 2003.

[35] K. Matsuda, Y. Sakaguchi, Y. Miyata, Y. Uetani, T. Sato, A. Kamio, and S. Ikeno. Precipitation sequence of various kinds of metastable phases in Al-1.0mass% $Mg_2Si$-0.4mass% Si alloy. *Journal of Materials Science*, 35(1):179–189, 2000.

[36] C. D. Marioara, H. Nordmark, S. J. Andersen, and R. Holmestad. Post-$\beta''$ phases and their influence on microstructure and hardness in 6xxx Al-Mg-Si alloys. *Journal of Materials Science*, 41(2):471–478, 2006.

[37] S. J. Andersen, C. D. Marioara, A. Frøseth, R. Vissers, and H. W. Zandbergen. Crystal structure of the orthorhombic U2-$Al_4Mg_4Si_4$ precipitate in the Al-Mg-Si alloy system and its relation to the $\beta'$ and $\beta''$ phases. *Materials Science and Engineering: A*, 390(1-2):127–138, 2005.

[38] R. W. G. Wyckoff. *Crystal structures*. Interscience, New York, 2nd edition, 1963.

[39] K. Matsuda, S. Tada, and S. Ikeno. The morphology of precipitates in an Al-1 wt *Journal of Electron Microscopy*, 42(1):1–6, 1993.

[40] C. Cayron and P. A. Buffat. Transmission electron microscopy study of the $\beta'$ phase (Al-Mg-Si alloys) and *qc* phase (Al-Cu-Mg-Si alloys): ordering mechanism and crystallographic structure. *Acta Materialia*, 48(10):2639–2653, 2000.

[41] K. Matsuda, S. Tada, H. Anada, Y. Uetani, and S. Ikeno. HREM observation of rod-shaped precipitates in an Al-1%$Mg_2Si$ alloy. In C. Q. Chen and E. A. Starke Jr., editors, *Aluminium alloys '90*, pages 486–491. International Academic Publishers, 1990.

[42] K. Matsuda, S. Tada, S. Ikeno, T. Sato, and A. Kamio. Crystal system of rod-shaped precipitates in an Al-1.0mass%$Mg_2Si$-0.4mass%Si alloy. *Scripta Metallurgica et Materialia*, 32(8):1175–1180, 1995.

[43] A. G. Frøseth, R. Høier, P. M. Derlet, S. J. Andersen, and C. D. Marioara. Bonding in MgSi and Al-Mg-Si compounds relevant to Al-Mg-Si alloys. *Physical Review B*, 67(22):224106, 2003.

[44] D. J. Chakrabarti and D. E. Laughlin. Phase relations and precipitation in Al-Mg-Si alloys with Cu additions. *Progress in Materials Science*, 49(3-4):389–410, 2004.

[45] S. D. Dumolt, D. E. Laughlin, and J. C. Williams. Formation of a modified $\beta'$ phase in aluminum alloy 6061. *Scripta Metallurgica*, 18(12):1347–1350, 1984.

[46] L. Sagalowicz, G. Lapasset, and G. Hug. Transmission electron microscopy study of a precipitate which forms in the Al-Mg-Si system. *Philosophical Magazine Letters*, 74(2):57–66, 1996.

[47] C. Ravi and C. Wolverton. First-principles study of crystal structure and stability of Al-Mg-Si-(Cu) precipitates. *Acta Materialia*, 52(14):4213–4227, 2004.

[48] L. Arnberg and B. Aurivillius. The crystal structure of $Al_xCu_2Mg_{12-x}Si_7$, (h-AlCuMgSi). *Acta Chemica Scandinavica A*, 34(1):1–5, 1980.

[49] L. Sagalowicz, G. Hug, D. Bechet, P. Sainfort, and G. Lapasset. A study of the structural precipitation in the Al-Mg-Si-Cu system. In *International Conference on Aluminium Alloys 4*, volume I, pages 636–643, Georgia, Atlanta, 1994. Trans Tech.

[50] C. Cayron, L. Sagalowicz, O. Beffort, and P. A. Buffat. Structural phase transition in Al-Cu-Mg-Si alloys by transmission electron microscopy study on an Al-4 wt% Cu-1 wt% Mg-Ag alloy reinforced by SiC particles. *Philosophical Magazine A*, 79(11):2833–2851, 1999.

[51] K. Matsuda, Y. Uetani, T. Sato, and S. Ikeno. Metastable phases in an Al-Mg-Si alloy containing copper. *Metallurgical and Materials Transactions a-Physical Metallurgy and Materials Science*, 32(6):1293–1299, 2001.

[52] C. Wolverton. Crystal structure and stability of complex precipitate phases in Al-Cu-Mg-(Si) and Al-Zn-Mg alloys. *Acta Materialia*, 49(16):3129–3142, 2001.

[53] F. King. *Aluminium and its alloys*. Ellis Horwood Ltd., Chichester, England, 1987.

[54] C. Cayron and P. A. Buffat. Structural phase transition in Al-Cu-Mg-Si and Al-Mg-Si alloys: Ordering mechanisms and crystallographic structures. In *Aluminium Alloys: Their Physical and Mechanical Properties, Pts 1-3*, volume 331-3 of *Materials Science Forum*, pages 1001–1006. Trans Tech Publications Ltd, Zurich-Uetikon, 2000.

[55] E. Hornbogen, A. K. Mukhopadhyay, and E. A. Starke. Precipitation hardening of Al-(Si, Ge) alloys. *Scripta Metallurgica et Materialia*, 27(6):733–738, 1992.

[56] A. Mukhopadhyay. Influence of Cu additions on the morphology of GeSi precipitates in an Al-Ge-Si alloy. *Metallurgical and Materials Transactions A*, 32(8):1949–1958, 2001.

[57] Y. Du, Y. A. Chang, B. Huang, W. Gong, Z. Jin, H. Xu, Z. Yuan, Y. Liu, Y. He, and F. Y. Xie. Diffusion coefficients of some solutes in fcc and liquid Al: critical evaluation and correlation. *Materials Science and Engineering A*, 363(1-2):140–151, 2003.

[58] A. Lutts. Pre-precipitation in Al–Mg–Ge and Al–Mg–Si. *Acta Metallurgica*, 9(6):577–586, 1961.

[59] S. Ceresara and P. Fiorini. Clustering in Al–Mg–Ge alloy. *Materials Science and Engineering*, 3(3):170–174, 1968.

[60] H. Suzuki, M. Kanno, and G. Itoh. Aging phenomena of Al-Mg-Ge alloys. *Journal of Japan Institute of Light Metals*, 31(4):232–239, 1981.

[61] K. Matsuda, S. Ikeno, and T. Munekata. HRTEM study of precipitates in Al-Mg-Si and Al-Mg-Ge alloys. *Materials Science Forum*, 519-521:221–225, 2006.

[62] K. Matsuda, T. Munekata, and S. Ikeno. Effect of Mg content on the precipitation in Al-Mg-Ge alloys. *Materials Science Forum*, 561-565:2049–2052, 2007.

[63] S. P. Ringer, K. S. Prasad, and G. C. Quan. Internal co-precipitation in aged Al-1.7Cu-0.3Mg-0.1Ge (at.%) alloy. *Acta Materialia*, 56(9):1933–1941, 2008.

[64] J. J. Thomson. Cathode rays. *Philosophical Magazine Series 5*, 44(269):293–316, 1897.

[65] H. Busch. Berechnung der Bahn von Kathodenstrahlen im axialsymmetrischen elektromagnetischen Felde. *Annalen der Physik*, 81:974–993, 1926.

[66] M. De Graef. *Introduction to conventional transmission electron microscopy*. Cambridge University Press, Cambridge, 2003.

[67] R. Erni. *Aberration-Corrected Imaging in Transmission Electron Microscopy: An Introduction*. Imperial College Press, 2010.

[68] O. Scherzer. Über einige Fehler von Elektronenlinsen. *Zeitschrift für Physik*, 101(9-10):593–603, 1936.

[69] H. Rose. Outline of a spherically corrected semiaplanatic medium-voltage transmission electron-microscope. *Optik*, 85(1):19–24, 1990.

[70] M. Haider, S. Uhlemann, E. Schwan, H. Rose, B. Kabius, and K. Urban. Electron microscopy image enhanced. *Nature*, 392(6678):768–769, 1998.

[71] B. Fultz and J. Howe. *Transmission electron microscopy and diffractometry of materials*. Springer, Berlin, 3rd edition, 2008.

[72] H. Bethe. Theorie der Beugung von Elektronen an Kristallen. *Annalen der Physik*, 87:55–129, 1928.

[73] C. J. Humphreys. The scattering of fast electrons by crystals. *Reports on Progress in Physics*, 42(11):1825–1887, 1979.

[74] E. J. Kirkland. *Advanced Computing in Electron Microscopy*. Springer, New York, 2nd edition, 2010.

[75] O. Scherzer. The theoretical resolution limit of the electron microscope. *Journal of Applied Physics*, 20(1):20–29, 1949.

[76] M. V. Sidorov. ctfExplorer, 2002. `http://clik.to/ctfexplorer`.

[77] M. Lentzen. Contrast transfer and resolution limits for sub-angstrom high-resolution transmission electron microscopy. *Microscopy and Microanalysis*, 14(01):16–26, 2008.

[78] D. B. Williams and C. B. Carter. *Transmission Electron Microscopy*. Plenum Press, New York, 1996.

[79] J. C. H. Spence and J. M. Cowley. Lattice imaging in STEM. *Optik*, 50(2):129–142, 1978.

[80] S.J. Pennycook, D.E. Jesson, M.F. Chisholm, N.D. Browning, A.J. McGibbon, and M.M. McGibbon. Z-contrast imaging in the scanning transmission electron microscope. *Microscopy and Microanalysis*, 1(01):231–251, 1995.

[81] P. D. Nellist. The principles of STEM imaging. In S. J. Pennycook and P. D. Nellist, editors, *Scanning transmission electron microscopy*. Springer, New York, 2011.

[82] J. Spence and J. M. Zuo. *Electron Microdiffraction*. Plenum, New York, 1992.

[83] J. M. Cowley and A. F. Moodie. The scattering of electrons by atoms and crystals. I. a new theoretical approach. *Acta Crystallographica*, 10(10):609–619, 1957.

[84] C. Dwyer. Simulation of scanning transmission electron microscope images on desktop computers. *Ultramicroscopy*, 110(3):195–198, 2010.

[85] R. F. Loane, P. Xu, and J. Silcox. Thermal vibrations in convergent-beam electron diffraction. *Acta Crystallographica Section A*, 47(3):267–278, 1991.

[86] L. J. Allen, S. D. Findlay, and M. P. Oxley. Simulation and interpretation of images. In S. J. Pennycook and P. D. Nellist, editors, *Scanning transmission electron microscopy*. Springer, New York, 2011.

[87] C. Dwyer, R. Erni, and J. Etheridge. Measurement of effective source distribution and its importance for quantitative interpretation of STEM images. *Ultramicroscopy*, 110(8):952–957, 2010.

[88] J. M. LeBeau, S. D. Findlay, L. J. Allen, and S. Stemmer. Quantitative atomic resolution scanning transmission electron microscopy. *Physical Review Letters*, 100(20):206101–4, 2008.

[89] J. M. LeBeau and S. Stemmer. Experimental quantification of annular dark-field images in scanning transmission electron microscopy. *Ultramicroscopy*, 108(12):1653–1658, 2008.

[90] J. M. LeBeau, S. D. Findlay, L. J. Allen, and S. Stemmer. Position averaged convergent beam electron diffraction: Theory and applications. *Ultramicroscopy*, 110(2):118–125, 2010.

[91] C. D. Marioara, S. J. Andersen, H. W. Zandbergen, and R. Holmestad. The influence of alloy composition on precipitates of the Al-Mg-Si system. *Metallurgical and Materials Transactions A*, 36(3):691–702, 2005.

[92] S. Andersen. Quantification of the $Mg_2Si$ $\beta''$ and $\beta'$ phases in AlMgSi alloys by transmission electron microscopy. *Metallurgical and Materials Transactions A*, 26(8):1931–1937, 1995.

[93] A. P. Sutton and R. W. Balluffi. *Interfaces in crystalline materials*. Clarendon Press, Oxford, 2006.

[94] W. Z. Zhang and G. C. Weatherly. On the crystallography of precipitation. *Progress in Materials Science*, 50(2):181–292, 2005.

[95] H. X. Gao and L. M. Peng. Parameterization of the temperature dependence of the Debye-Waller factors. *Acta Crystallographica Section A*, 55:926–932, 1999.

# Part II

# Papers

# Paper I

## Precipitation in two Al-Mg-Ge alloys

R. Bjørge, C. D. Marioara, S. J. Andersen and R. Holmestad

Metallurgical and Materials Transactions A 41 (2010) 1907–1916.

Is not included due to copyright

# Paper II

## Precipitates in an Al-Mg-Ge alloy studied by aberration-corrected scanning transmission electron microscopy

R. Bjørge, P. N. H. Nakashima, C. D. Marioara, S. J. Andersen, B. C. Muddle, J. Etheridge and R. Holmestad

Acta Materialia 59 (2011) 6103–6109.

Available online at www.sciencedirect.com
ScienceDirect
Acta Materialia 59 (2011) 6103–6109
Acta MATERIALIA
www.elsevier.com/locate/actamat

# Precipitates in an Al–Mg–Ge alloy studied by aberration-corrected scanning transmission electron microscopy

R. Bjørge [a], P.N.H. Nakashima [b,c], C.D. Marioara [d], S.J. Andersen [d], B.C. Muddle [b,c], J. Etheridge [e,c], R. Holmestad [a,*]

[a] Department of Physics, Norwegian University of Science and Technology (NTNU), 7491 Trondheim, Norway
[b] ARC Centre of Excellence for Design in Light Metals, Monash University, Victoria 3800, Australia
[c] Department of Materials Engineering, Monash University, Victoria 3800, Australia
[d] Department of Synthesis and Properties, SINTEF Materials and Chemistry, 7465 Trondheim, Norway
[e] Monash Centre for Electron Microscopy, Monash University, Victoria 3800, Australia

Received 17 February 2011; received in revised form 9 June 2011; accepted 13 June 2011
Available online 19 July 2011

**Abstract**

The precipitates present in an Al–0.59Mg–0.71Ge (at.%) alloy have been studied using aberration-corrected high-angle annular dark-field scanning transmission electron microscopy. Two types of needle-shaped precipitates growing along $\langle 0\,0\,1\rangle_{Al}$ were found: a phase isostructural to the trigonal U1 phase found in Al–Mg–Si alloys, and finer precipitates with a hexagonal arrangement of Ge columns. The study revealed the presence of a complex interface structure surrounding the U1-like precipitates, and an explanation based on interatomic distances is proposed.


*Keywords:* Al alloys; Precipitation; STEM HAADF; Interface structure; Al–Mg–Si alloys

## 1. Introduction

Al–Mg–Ge alloys have been shown to share similarities with the industrially important Al–Mg–Si(–Cu) alloys [1–3]. Some of the precipitate phases known from the Al–Mg–Si system have isostructural counterparts in Al–Mg–Ge, specifically the trigonal U1 phase ($a = b = 0.405$ nm, $c = 0.674$ nm, $\gamma = 120°$) [4] (also known as type-A or $\beta'_A$ [5]) and the hexagonal β′ phase ($a = b = 0.715$ nm, $c = 0.405$ nm, $\gamma = 120°$) [6]. These two phases play a more important role in precipitation-hardening in the Al–Mg–Ge alloys than in the Al–Mg–Si system [1]. An isostructural counterpart to the β″ phase, the most important hardening phase in the Al–Mg–Si alloy system, was not observed in Al–Mg–Ge, yet these alloys reach hardnesses similar to those of comparable Al–Mg–Si alloys. In the present work, precipitates in the Ge-rich alloy in [1] are studied using aberration-corrected high-angle annular dark-field scanning transmission electron microscopy (HAADF STEM).

In Ref. [1], it was shown that a U1-like phase forms in this alloy (therefore called U1-Ge), as well as precipitates of an indeterminate phase. Both precipitate types are needle-shaped, grow in the $\langle 0\,0\,1\rangle_{Al}$ direction, and are coherent with the matrix in this direction. The needle cross-section is typically elongated along one $\langle 1\,0\,0\rangle_{Al}$ direction, with almost planar interfaces between precipitate and matrix parallel to this elongation direction. The U1 precipitates are finer in the Al–Mg–Ge alloy than in the corresponding Al–Mg–Si alloy. The *c*-axis of the U1-Ge unit cell in most of the precipitates was found to lie close to $\langle 2\,1\,0\rangle_{Al}$. This is different from U1 in Al–Mg–Si, where the *c*-axis is parallel to $\langle 3\,1\,0\rangle_{Al}$ and where the cross-section is not elongated [4]. A $\langle 1\,1\,0\rangle_{U1}$ direction is parallel with the needle direction in both the Al–Mg–Si and Al–Mg–Ge systems.

* Corresponding author. Tel.: +47 73593173, fax: +47 73597710.
*E-mail address:* randi.holmestad@ntnu.no (R. Holmestad).

1359-6454/$36.00 © 2011 Acta Materialia Inc. Published by Elsevier Ltd. All rights reserved.
doi:10.1016/j.actamat.2011.06.021

Ref. [1] left several questions unanswered. The position of the atoms in the U1-Ge unit cell could not be determined unambiguously due to limited resolution, i.e. it was not possible to distinguish between two mirror images of the structure. In addition, the detailed nature of the precipitate/matrix interface was not resolved. Some HAADF STEM images showed an increased intensity at the interface protruding into the matrix at semi-regular intervals. A better knowledge of the precipitate/matrix interface could help to explain why the U1 phase behaves differently in the Al–Mg–Ge alloy.

The strong atomic number dependence of HAADF STEM images makes it possible to distinguish between Ge ($Z = 32$) columns and Mg or Al ($Z = 12$, 13) columns. Furthermore, intensity peaks in the HAADF STEM image correspond directly to atomic column positions. This makes the qualitative interpretation of these images less ambiguous than, for example, high-resolution transmission electron microscopy images [7]. This is particularly important when studying interfaces and defects [8]. In this work, we make use of state-of-the-art aberration-corrected microscopy in order to reveal more of the detailed structure of precipitates in the Al–Mg–Ge alloy.

## 2. Methods

An Al–0.59 Mg–0.71Ge (at.%) alloy was cast and homogenized for 4 h at 550 °C, before being extruded. The alloy was subsequently solution heat treated for 2 h at 600 °C, water quenched to room temperature and held for 4 h, followed by ageing at 200 °C for 16 h and water quenching to room temperature. TEM samples were prepared by twin-jet electropolishing with a 33% nitric acid/67% methanol solution at −20 °C with a voltage of 13 V. HAADF STEM images were acquired at Monash University on an FEI Titan$^3$ 80-300 FEG-TEM operating at 300 kV and equipped with aberration correctors (CEOS GmbH) for both the probe-forming and image-forming lenses. The probe convergence semi-angle in STEM mode was 15 mrad, as measured from the corresponding convergent-beam electron diffraction pattern. The inner angle of the HAADF detector was 40 mrad and the outer angle of the order of 200 mrad. HAADF STEM simulations were performed using the program stemimg [9].

## 3. Results and discussion

### 3.1. U1-Ge

An unprocessed HAADF STEM image of a U1-like precipitate viewed along $\langle 0\,0\,1\rangle_{Al}$ is shown in Fig. 1a. The logarithm of the modulus of the fast Fourier transform (FFT) of this image is shown in Fig. 1b. A low-pass filtered version of Fig. 1a with atomic overlay is shown in Fig. 1c. Spatial frequencies beyond the circle shown in Fig. 1b, corresponding to distances smaller than 0.12 nm, were excluded in Fig. 1c in order to reduce the amount of noise. The same filter was applied to obtain all the filtered images in this work. The Ge columns appear as the brightest spots in the precipitate. The arrangement resembles a deformed hexagonal net. Rows of Mg columns are also clearly resolved in most of the precipitate. These form a bright band in between the rows of Ge columns. The Al columns of the precipitate can be seen as intensity extending out from the Ge columns. The space between the Al columns forms a darker band. This atomic configuration, superimposed in Fig. 1c, is in perfect agreement with the U1 model [1,4], with Ge on Si sites. The mirror image of the superimposed unit cell (i.e. the unit cell flipped about the *c*-axis) does not fit this precipitate. Thus, the orientation of the atomic contents of the unit cell with respect to the matrix, which could not be resolved in Ref. [1], has been determined. All but one of the U1-Ge precipitates observed in the analyzed condition had the same orientation. In this orientation, the Al columns are aligned parallel with $\langle 1\,0\,0\rangle_{Al}$ and the largest interface.

Interestingly, one precipitate with the U1 structure was observed that had the alternative unit cell orientation (Fig. 2), i.e. the row of Al columns is not aligned with the interface. The FFT in Fig. 2b shows some of the spots associated with U1-Ge seen in Fig. 1b. An atomic model is overlaid in the Fourier-filtered image in Fig. 2c. One can see that the precipitate is not completely ordered. The Mg and Al columns were determined based on the similarity with ordered U1-Ge and the known interatomic spacings there. The rhombuses that are drawn with yellow lines contain two Al columns in the U1 structure. Here, in parts of the precipitate they contain Al and Mg instead. Despite the deviation from the U1 structure, the left part of the precipitate, enclosed by red lines, does have an approximate 2-fold rotational symmetry.

This precipitate is noticeably smaller than the other U1-Ge precipitates. The less common orientation must be less energetically favourable because of the different precipitate–matrix interface. If first stabilized, such precipitates would find growth more difficult, and end up smaller.

### 3.2. The U1-Ge/matrix interface

In Fig. 1, it can be seen that the Ge columns form slight zigzag lines parallel to the cross-section elongation direction, and hence, a $\langle 1\,0\,0\rangle_{Al}$ direction. The $(1\,\bar{1}\,1)_{U1}$ planes are parallel to the $(0\,2\,0)_{Al}$ planes of the matrix (as shown in Fig. 1c).

A noticeable feature of the U1-Ge precipitates is the bright columns appearing in the two largest interfaces at semi-regular intervals. They do not lie on matrix positions nor are they a continuation of the U1 structure. They are specific to this precipitate/matrix interface. The 2-fold rotational symmetry of the precipitate is also striking. Not only does the U1 structure have 2-fold symmetry in this projection, but here the precipitate morphology and the presence of the bright columns at the interface also obey this 2-fold symmetry.

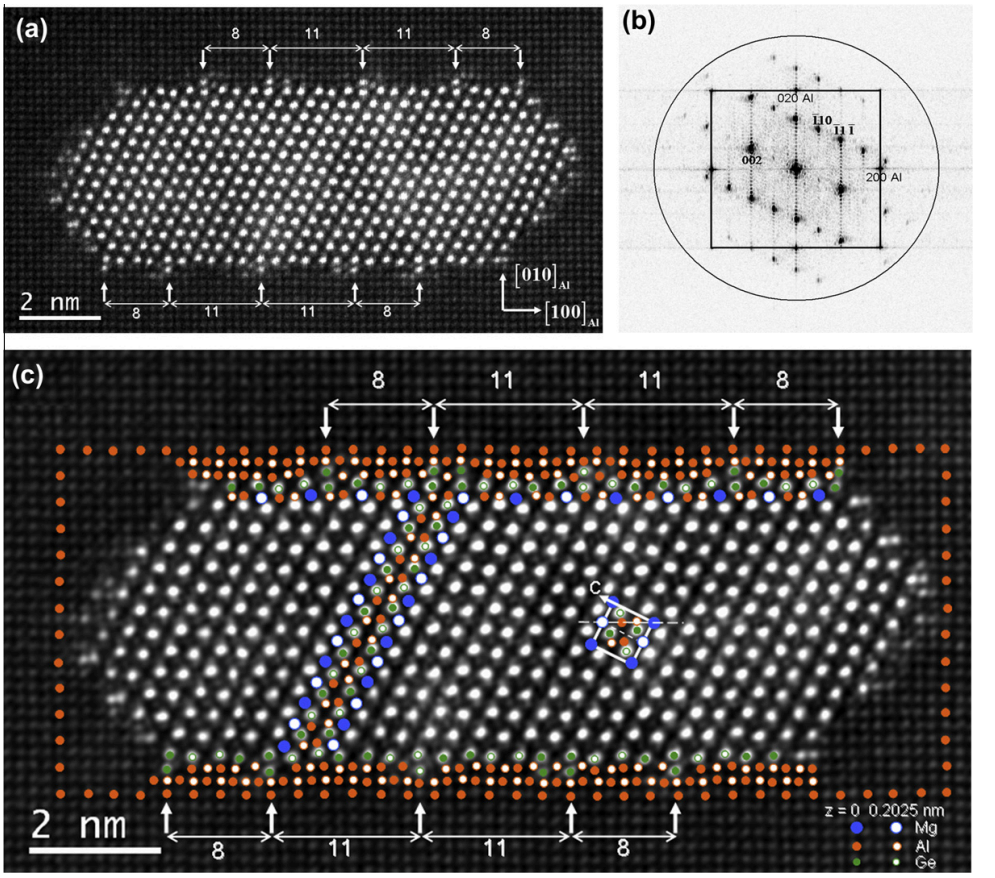


Fig. 1. (a) Unfiltered HAADF STEM image of a U1-Ge precipitate. The intensity of the brightest pixels has been clipped by setting the grey levels of the image in order to make the dimmer atomic columns more visible. The number of $(2\,0\,0)_{Al}$ planes between the extra Ge columns at the interface is indicated. (b) FFT of the image in (a). Some of the intensity peaks due to the precipitate and the matrix have been indexed according to a $[1\,1\,0]_{U1}/[0\,0\,1]_{Al}$ zone axis. A square connects the spots due to the Al matrix. (c) Filtered version of (a) with a U1-Ge unit cell and atomic model superimposed. Filled and unfilled circles in the atomic model correspond to the two different layers of the structure, which are separated by 0.2025 nm along $[0\,0\,1]_{Al}$. A trace of a $(1\,\bar{1}\,1)_{U1}$ plane is also shown (horizontal dashed line).

Strain can affect HAADF intensity through dechannelling of the electron probe. We therefore investigated whether these high-intensity columns could be due to straining of the Al matrix. STEM simulations were performed where the atoms in one Al matrix column at the precipitate/matrix interface were displaced perpendicular to the incident beam direction, with the amplitude of the displacement varying sinusoidally as a function of depth, as in Ref. [10]. The size of the supercell used in the calculation was $3.3 \times 3.3\ nm^2$. Aberrations were set to zero.

These simulations showed that strain of this form can lead to a decrease in the intensity of the Al column, but not to an increase. In addition, the simulated strain in one column did not lead to higher intensity in any neighbouring columns. Therefore, the bright columns near the interface seen in these images must contain Ge. These "extra" Ge columns often have less intensity than the Ge columns in the bulk of the precipitate. This could be due to intermixing of Ge and Al and/or Mg in the column, vacancies, strain, dechannelling into lighter neighbouring columns or a combination of these factors.

The extra Ge columns either occur singly, exclusively where the zigzag line of Ge columns points into the precipitate, or in pairs, with one column occurring where the zigzag line points into the precipitate and one adjacent to this, where the zigzag points away from the precipitate. Extra Ge columns that occur where the zigzag points away from the precipitate are dimmer than the other extra Ge columns, or else neither an extra Ge column nor a matrix column are visible, presumably due to a lack of space. The spacing between extra Ge columns next to where the zigzag points into the precipitate is always either 8 or 11 $(2\,0\,0)_{Al}$ planes, as shown in Fig. 1a. The periodic occurrence of these Ge columns suggests that they appear at specific sites.

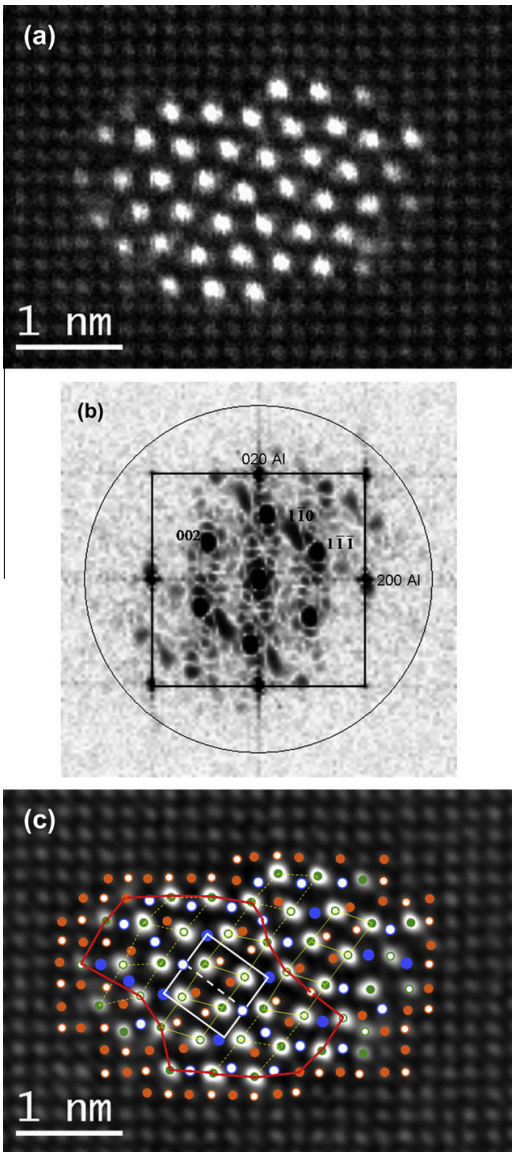


Fig. 2. (a) HAADF STEM image of a U1-Ge precipitate with a different unit cell orientation. (b) FFT of the image in (a). The same intensity peaks as in Fig. 1b have been indexed, but according to a $[\bar{1}\ \bar{1}\ 0]_{U1}$ zone axis. A square connects the spots due to the Al matrix. (c) Filtered version of (a) with a U1-Ge unit cell and atomic model overlaid. The thick line encloses a part of the precipitate that has an approximate 2-fold rotational symmetry. See Fig. 1c for legend.

In Fig. 3, a model of this U1/matrix interface is drawn. Only the terminating layer of Ge columns and two planes of matrix columns are shown. Both the U1 and Al matrix structures consist of two different layers of atoms separated by 0.2025 nm along the needle direction, and are coherent along this direction. The columns along the needle direction

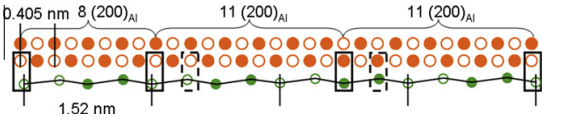


Fig. 3. Model of an idealized U1 (bottom)/matrix (top) interface. Areas where neighbouring columns either side of the interface have atoms at the same height are enclosed by rectangles, drawn with full lines where the zigzag of Ge columns points into the precipitate and dashed lines where the zigzag points away from the precipitate. The repeat distances of the Al matrix and U1 along the interface are shown. See Fig. 1c for legend.

are staggered so that neighbouring columns are offset by 0.2025 nm along this direction. It can be seen in Fig. 3 that areas where neighbouring columns on opposite sides of the interface have atoms at the same height occur with exactly the same periodicity as the extra Ge columns in the image. This is independent of the relative alignment of the two structures. We see in Fig. 1c that the extra Ge columns only occur where the matrix column is right next to a precipitate Ge column with atoms at the same height.

We therefore conclude that the extra Ge columns form exactly at these sites, where the interatomic distances across the interface are small. The measured (projected) distance between the extra Ge columns and the neighbouring precipitate Ge columns is on average 0.24 nm, similar to the length of a covalent Ge–Ge bond. The reason for the formation of extra Ge columns at these sites is, however, not known. Replacing a matrix column with Ge could be favourable due to the size difference between Al and Ge, or short Ge–Ge bonds might be favoured over short Al–Ge bonds. Density functional theory calculations might be able to explain why this interface structure is energetically favourable. At any rate, the more coherent interface in these precipitates probably hinders coarsening and also makes the U1-Ge precipitates contribute more to the precipitation hardening, through a larger strain field, than is the case for the coarser and more incoherent U1 precipitates in Al–Mg–Si alloys.

The repeat distance for U1 along the cross-section elongation is 1.52 nm, while the lattice parameter of Al is 0.405 nm. This means that there will be near coincidence every four repeat distances of U1, corresponding to 15 Al unit cells, or 30 $(2\,0\,0)_{Al}$ planes (6.08 nm). This is also what we observe in Fig. 1, with the spacing between the extra Ge columns being 11, 11 and 8 $(2\,0\,0)_{Al}$ planes $(11 + 11 + 8 = 30)$. The interfaces of other U1-Ge precipitates did not all have this 6.08 nm periodicity, but the distance between these extra Ge columns is always 8 or 11 $(2\,0\,0)_{Al}$ planes.

### 3.3. Needles with a hexagonal Ge network

The second type of precipitate phase that formed in this alloy were needles with smaller cross-sections and a hexagonal arrangement of the Ge columns when viewed along the needle direction (Fig. 4). The cross-section is always

elongated along a $\langle 1\,0\,0\rangle_{Al}$ type direction and the precipitates are coherent with the matrix in the interface plane with trace parallel to the cross-section elongation. A $\langle 1\,1\,0\rangle$-type direction of the hexagonal subcell that makes up the network of Ge columns is equal to $\langle 1\,0\,0\rangle_{Al}$ (see Fig. 4a).

One example of this type is shown in Fig. 4a–c. In Fig. 4c, a likely atomic model has been superimposed on

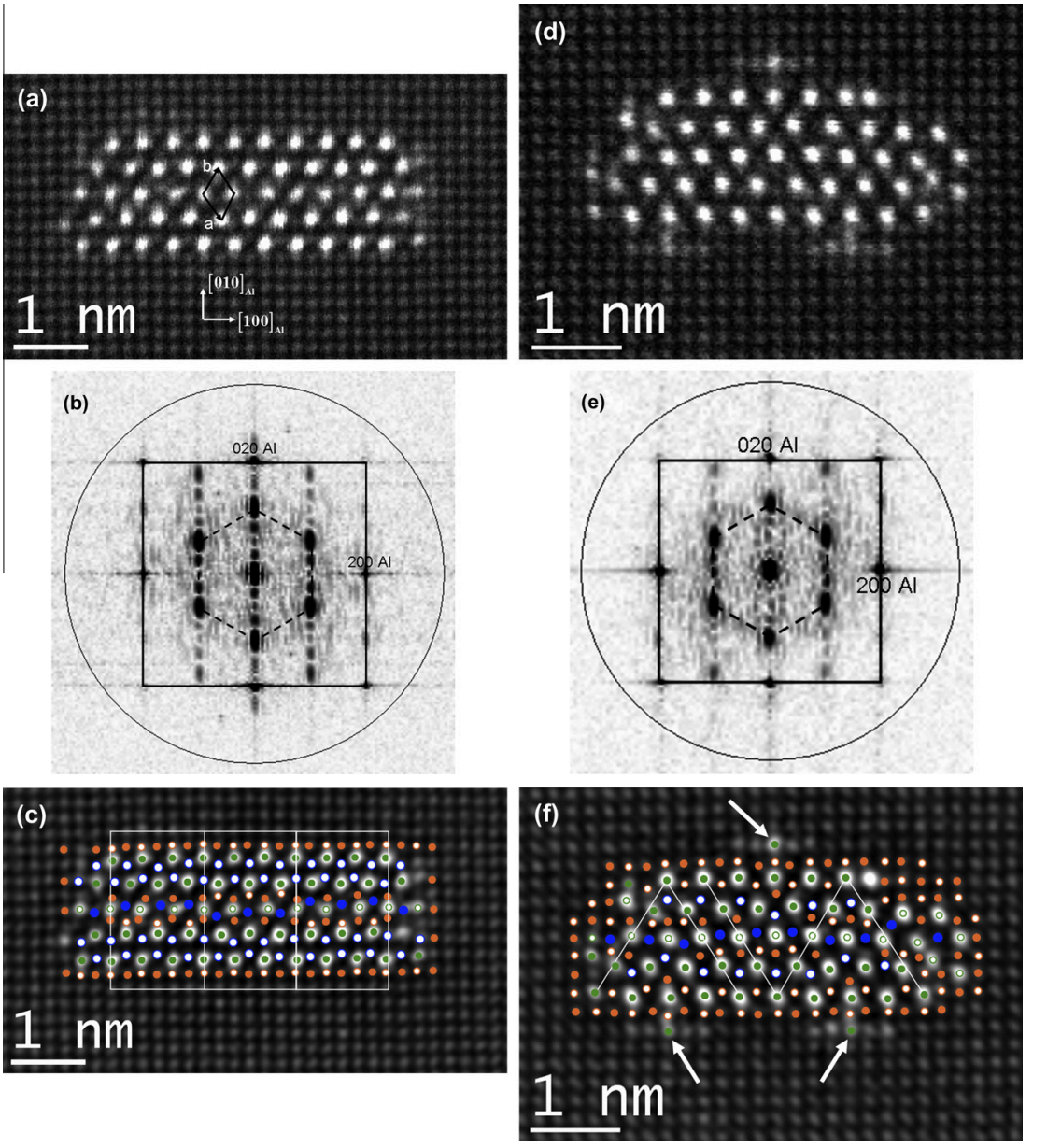


Fig. 4. HAADF STEM images of precipitates with a hexagonal arrangement of Ge columns. The spots in the FFTs due to this hexagonal Ge network are connected by dashed lines. A square connects the spots due to the Al matrix. (a) Unfiltered image of such a precipitate. The lattice directions in the matrix and the hexagonal subcell of the Ge columns are indicated. (b) FFT of (a). (c) Filtered version of (a). An atomic model is superimposed. The repeating rectangular building blocks are indicated. (d) Unfiltered image of another example of this type of precipitate. (e) FFT of (d). (f) Filtered version of (d). An atomic model is superimposed. The extra Ge-rich columns in the matrix and the triangular building blocks are indicated. See Fig. 1c for legend.

the filtered image. The Ge-rich columns are easily identified based on the image intensity, but it is practically impossible to distinguish between Mg and Al based on intensity. The distances between atomic columns in the image, taking into account the heights of the atoms in the columns, were therefore compared with interatomic distances determined from the respective elemental phases. These interatomic distances have been found to lie close to the true interatomic distances in precipitates in Al–Mg–Si alloys [4,11]. Nevertheless, some of the columns labelled as Mg could be Al, and vice versa.

Based on the arrangement of the Mg and Al columns around the Ge columns of the precipitate, the precipitate can be divided into smaller "building blocks" that make up most of the precipitate. These rectangular blocks have been drawn in Fig. 4c. They are related to each other through a 2-fold rotation or a flip.

Another example is shown in Fig. 4d–f. One can observe Ge in some of the matrix columns adjacent to the interface (indicated by arrows in Fig. 4f). These columns probably contain a mixture of Ge and Al or Mg since they are dimmer than the Ge columns in the precipitate. They are reminiscent of the extra Ge columns observed at the interface of U1-Ge, but here they occur farther into the matrix, and moreover the spacing between the extra Ge columns is different. It is also noted that these extra Ge columns consist of a central bright Ge-containing column with two atomic columns on either side parallel to the interface that also appear more intense than the Al matrix columns, although not as intense as the central Ge-containing column. These brighter columns only appear parallel to the interface and not above or below the central Ge-containing column, suggesting the increase in intensity is due to composition, rather than strain or electron scattering effects. Due to the differences between the Ge-rich matrix columns surrounding this precipitate and the U1-Ge precipitates, it is possible that the underlying causes are also different. That is, in the precipitate in Fig. 4d–f the extra Ge columns are probably not due to small interatomic spacings.

A likely atomic model has been superimposed according to the principles outlined above. Based on the arrangement of the Mg and Al columns around the Ge columns of the precipitate, combined with the extra Ge columns at the interface, the precipitate can be divided into three triangular parts that are related through a 2-fold rotation or flip, although here a fault separates two of these building blocks.

Thus, these precipitates with a hexagonal arrangement of Ge columns when viewed along the needle direction consist of symmetry-related blocks or structural units. They do not appear to contain a unit cell. This is different from the Al–Mg–Si system, where precipitates typically consist of one crystallographic phase or contain different phases in different parts of the precipitate that are only related through a common network of Si columns [11]. These results are somewhat similar to the findings of Kovarik et al. [12] in an Al–Cu–Mg alloy, where needle-like precipitates present after prolonged ageing were also found to consist of repeating structural units, with no apparent unit cell.

## 4. Conclusions

Precipitates in an Al–0.59 Mg–0.71Ge (at.%) alloy were investigated using aberration-corrected HAADF STEM. There were two main types: precipitates with a U1-like structure, and smaller precipitates with a hexagonal arrangement of the Ge columns. Both types were needle-shaped with cross-sections elongated along one $\langle 1\,0\,0\rangle_{Al}$ direction.

In the case of the U1-Ge precipitates, this orientation aligns rows of both Al and Ge columns in the precipitate with the surrounding matrix, leading to a partially coherent interface. The precipitate is terminated at the two largest interfaces by a zigzag line of Ge columns. Due to the structural mismatch, the interface cannot be completely coherent. A column consisting mainly of Ge atoms forms at the interface where atoms of two neighbouring columns at each side of the interface are at the same height and the zigzag points into the precipitate. Where two neighbouring columns are at the same height and the zigzag points away from the precipitate, an extra Ge column forms or the column is absent.

In the case of the smaller non-U1 precipitates, the interface is more coherent. No unit cell was observed for these precipitates, but they could be divided into smaller symmetry-related blocks.

## Acknowledgements

R.B., C.D.M., S.J.A. and R.H. were supported by Hydro, Steertec Raufoss and the Research Council of Norway through Project No. 176816/I40. R.B. and P.N.H.N. would like to thank Dr. Matthew Weyland and Dr. Christian Maunders for expert advice on use of the FEI Titan$^3$ 80-300 FEG-TEM. R.B. would like to thank Dr. Christian Dwyer for advice on use of the program stemimg. The FEI Titan$^3$ 80-300 FEG-TEM was funded via the Australian Research Council infrastructure Grant LE0454166.

## References

[1] Bjørge R, Marioara CD, Andersen SJ, Holmestad R. Metall Mater Trans A 2010;41:1907.
[2] Matsuda K, Ikeno S, Munekata T. Mater Sci Forum 2006;519–521:221.
[3] Matsuda K, Munekata T, Ikeno S. Mater Sci Forum 2007;561–565:2049.
[4] Andersen SJ, Marioara CD, Vissers R, Frøseth A, Zandbergen HW. Mater Sci Eng A 2007;444:157.
[5] Matsuda K, Sakaguchi Y, Miyata Y, Uetani Y, Sato T, Kamio A, et al. J Mater Sci 2000;35:179.
[6] Vissers R, van Huis MA, Jansen J, Zandbergen HW, Marioara CD, Andersen SJ. Acta Mater 2007;55:3815.

[7] Nellist PD, Pennycook SJ. The principles and interpretation of annular dark-field Z-contrast imaging. Advances in imaging and electron physics, vol. 113. San Diego, CA: Academic Press; 2000. p. 147.
[8] Pennycook SJ, Jesson DE. Acta Metall Mater 1992;40:S149.
[9] Dwyer C. Ultramicroscopy 2010;110:195.
[10] Plamann T, Hÿtch MJ. Ultramicroscopy 1999;78:153.
[11] Andersen SJ, Marioara CD, Frøseth A, Vissers R, Zandbergen HW. Mater Sci Eng A 2005;390:127.
[12] Kovarik L, Court SA, Fraser HL, Mills MJ. Acta Mater 2008;56:4804.

# Paper III

## Scanning transmission electron microscopy investigation of an Al-Mg-Si-Ge-Cu alloy

R. Bjørge, S. J. Andersen, C. D. Marioara, J. Etheridge and R. Holmestad

Submitted to Philosophical Magazine.

Is not included due to copyright

# Paper IV

## Aberration-corrected scanning transmission electron microscopy study of $\beta'$-like precipitates in an Al-Mg-Ge alloy

R. Bjørge, C. Dwyer, M. Weyland, P. N. H. Nakashima, C. D. Marioara, S. J. Andersen, J. Etheridge and R. Holmestad

To be submitted.

Is not included due to copyright